GAUSSIAN BEAM METHODS FOR THE SCHRÖDINGER EQUATION IN THE SEMI-CLASSICAL REGIME: LAGRANGIAN AND EULERIAN FORMULATIONS*

SHI JIN†, HAO WU‡, AND XU YANG§

Abstract. The solution to the Schrödinger equation is highly oscillatory when the rescaled Planck constant ε is small in the semiclassical regime. A direct numerical simulation requires the mesh size to be $O(\varepsilon)$. The Gaussian beam method is an efficient way to solve the high frequency wave equations asymptotically, outperforming the geometric optics method in that the Gaussian beam method is accurate even at caustics.

In this paper, we solve the Schrödinger equation using both the Lagrangian and Eulerian formulations of the Gaussian beam methods. A new Eulerian Gaussian beam method is developed using the level set method based only on solving the (complex-valued) homogeneous Liouville equations. A major contribution here is that we are able to construct the Hessian matrices of the beams by using the level set function's first derivatives. This greatly reduces the computational cost in computing the Hessian of the phase function in the Eulerian framework, yielding an Eulerian Gaussian beam method with computational complexity comparable to that of the geometric optics but with a much better accuracy around caustics.

We verify through several numerical experiments that our Gaussian beam solutions are good approximations to Schrödinger solutions even at caustics. We also numerically study the optimal relation between the number of beams and the rescaled Planck constant ε in the Gaussian beam summation.

Key words. Schrödinger equation, Gaussian beam method, Liouville equation.

AMS subject classifications. 81Q20, 65M99.

1. Introduction

We are interested in the Gaussian beam methods for the numerical approximation of the Schrödinger equation:

$$i\varepsilon \frac{\partial \Psi^\varepsilon}{\partial t} + \frac{\varepsilon^2}{2}\Delta\Psi^\varepsilon - V(\boldsymbol{x})\Psi^\varepsilon = 0, \quad \boldsymbol{x}\in\mathbb{R}^n, \tag{1.1}$$

with the WKB initial data,

$$\Psi^\varepsilon(0,\boldsymbol{x}) = A_0(\boldsymbol{x})e^{iS_0(\boldsymbol{x})/\varepsilon}. \tag{1.2}$$

Here $\Psi^\varepsilon(\boldsymbol{x},t)$ is the wave function, ε is the re-scaled Plank constant, and $V(\boldsymbol{x})$ is a

†Department of Mathematics, University of Wisconsin, Madison, WI 53706, USA (jin@math.wisc.edu).

‡Department of Mathematical Sciences, Tsinghua University, Beijing, 10084, China (hwu04@mails.tsinghua.edu.cn).

§Department of Mathematics, University of Wisconsin, Madison, WI 53706, USA (xyang@math.wisc.edu).

smooth potential. The physical observables can be defined in terms of $\Psi^\varepsilon(\boldsymbol{x},t)$:

$$\text{position density} \quad n^\varepsilon = |\Psi^\varepsilon|^2, \tag{1.3}$$

$$\text{density flux} \quad J^\varepsilon = \frac{\varepsilon}{2i}(\Psi^\varepsilon \nabla \overline{\Psi^\varepsilon} - \overline{\Psi^\varepsilon} \nabla \Psi^\varepsilon), \tag{1.4}$$

$$\text{kinetic energy} \quad E^\varepsilon = \frac{\varepsilon^2}{2}|\nabla \Psi^\varepsilon|^2. \tag{1.5}$$

The wave function $\Psi^\varepsilon(\mathbf{x},t)$ and the related physical observables become oscillatory of wave length $O(\varepsilon)$ when ε is small — in the so-called semiclassical regime. A mesh size of $O(\varepsilon)$ is required when using the time-splitting spectral method [1] to simulate (1.1)–(1.2) directly. The mesh size (and the time step as well) becomes even worse, since they need to be as small as $o(\varepsilon)$, if finite difference methods are used [21, 22]. The mesh and time step restrictions of these methods make the computation of (1.1)–(1.2) extremely expensive, especially in high dimensions.

One alternative efficient approach is to solve the equation asymptotically by the classical WKB method. Applying the ansatz

$$\Psi^\varepsilon(t,\boldsymbol{x}) = A(t,\boldsymbol{x})e^{iS(t,\boldsymbol{x})/\varepsilon} \tag{1.6}$$

to (1.1), one obtains the eikonal equation for the phase $S(t,\boldsymbol{x})$ and the transport equation for the amplitude $\rho(t,\boldsymbol{x}) = |A(t,\boldsymbol{x})|^2$([34]):

$$S_t + \frac{1}{2}|\nabla S|^2 + V(\boldsymbol{x}) = 0, \tag{1.7}$$

$$\rho_t + \nabla \cdot (\rho \nabla S) = 0. \tag{1.8}$$

Since the eikonal equation is of the Hamilton-Jacobi type, the solution becomes singular after caustic formation. Beyond caustics, the correct semiclassical limit of the Schrödinger equation becomes multivalued. The multivalued solution can be computed by ray tracing methods [6, 2, 3], wave front methods [32, 9], moment methods [11, 14] and level set methods [16, 5, 15, 17]. We also refer the readers to the review paper on computational high frequency waves [8].

A problem with WKB or geometric optics based methods is that the asymptotic solution is invalid at caustics, since the amplitude $\rho(\boldsymbol{x},t)$ blows up there. None of the aforementioned methods could give accurate solutions near caustics. But, on the other hand, accurately computing the solutions around the caustics is important in many applications, for example, in seismic imaging [12, 13].

The Gaussian beam method, developed for high frequency linear waves, is an efficient approximate method that allows accurate computation of the wave amplitude around caustics [28]. Similar to the ray tracing method, the Gaussian beam solution also has a WKB form of (1.6). The ray determined by (1.7)–(1.8) is the center of the Gaussian beam. The difference lies in that the Gaussian beam allows the phase function $S(\boldsymbol{x},t)$ to be *complex* off its center, and the imaginary part of $S(\boldsymbol{x},t)$ is chosen so that the solution decays exponentially away from the center. The Lagrangian formulation consists of the ray tracing equations determined by (1.7)–(1.8), which describe the trajectory of the beam center, and the Riccati equation, which describes the Hessian of the phase $S(\boldsymbol{x},t)$. The validity of this construction at caustics is analyzed by Ralston in [29].

Lagrangian numerical methods of Gaussian beams are usually developed based on the Taylor expansion and superposition principle. The accuracy of the beam off

the central ray is determined by the truncation error of Taylor expansion, and the approximate solution is given by a sum of all the beams (see [4, 13, 25]). The accuracy of the Taylor expansion was studied by Motamed and Runborg [24], and Tanushev [30] developed and analyzed higher order Gaussian beams giving better accuracy of the approximations.

Compared to Lagrangian methods based on ray tracing, which lose accuracy when the ray diverges and need re-interpolation to maintain the numerical accuracy, which can be very complicated, Eulerian methods based on solving PDEs on fixed grids have the advantage of a uniform accuracy. Here we remark that the Lagrangian methods based on wave front constructions [32, 9, 25] do not suffer from the issue of ray divergence. Recently, motivated by the work of Tanushev, Qian and Ralston [31], Leung, Qian and Burridge [19] designed an Eulerian Gaussian beam summation method for the Helmholtz equations. In their formulation for n space dimensions, the Hessian matrix of the phase was solved by $2n^2$ *complex*-valued *inhomogeneous* Liouville equations.[1] They also introduced the semi-Lagrangian method to numerically evaluate the singular Eulerian beam summation integral.

In this paper we systematically study the Gaussian beam method for solving the Schrödinger equation in the semiclassical regime using both the Lagrangian and the Eulerian formulations. The Lagrangian formulation follows the classical work for linear hyperbolic equations [29]. The main contribution of this paper is a new Eulerian Gaussian beam method using the level set function. To compute the velocity and the Hessian of the phase, we only use n complex valued *homogeneous* level set Liouville equations, rather than $2n^2$ inhomogeneous complex valued Liouville equations for the Hessian in addition to n real-valued homogeneous Liouville equations for the velocity as in [19]. The Hessian of the phase is evaluated from the first derivatives of the level set functions. This new formulation significantly reduces the number of Liouville equations used to construct the Hessian of the phase. As a matter of fact, the computational method for the (complex-valued) phase and amplitude is not much different from the level set method used for geometric optics computations as in [5, 16, 15]. In addition, we also evaluate the Gaussian beam summation integral using the semi-Lagrangian method of [19] *only near* caustics, thus largely maintain the accuracy of the Eulerian method. This new method will be tested for its accuracy and efficiency by comparing with the solution of the Schrödinger Equation (1.1)–(1.2).

Note that when there are many caustics, which make the velocity contours rather complicated, the implementation of this local semi-Lagrangian method is difficult. In these cases we refer to a discretized delta function method [33] for numerically computing the Gaussian beam summation integral, which will be studied in a forthcoming work.

The paper is organized as follows. In Sec. 2, we introduce the Lagrangian Gaussian beam formulation and summarize its properties. In Sec. 3, we give a detailed derivation of the new level set formulations for the Eulerian Gaussian beam method. We also discuss how to implement the summation of the Eulerian Gaussian beams, with an analysis of the computational complexity of this new method at the end. The numerical examples are given in Sec. 4 to test the accuracy and efficiency of the Gaussian beam methods. We make some conclusive remarks in Sec. 5.

---

[1]After we completed this manuscript, we received reference [18], where the Eulerian Gaussian beam method of [19] was extended to the semiclassical Schrödinger equation still using the same formulations for the Hessian of the phase as in [19].

2. The Lagrangian formulation

In this section, we adopt the Gaussian beam approximation to the Schrödinger equation (1.1). Let

$$\varphi_{la}^{\varepsilon}(t,\boldsymbol{x},\boldsymbol{y}_0) = A(t,\boldsymbol{y})e^{iT(t,\boldsymbol{x},\boldsymbol{y})/\varepsilon}, \tag{2.1}$$

where $\boldsymbol{y} = \boldsymbol{y}(t,\boldsymbol{y}_0)$ and $T(t,\boldsymbol{x},\boldsymbol{y})$ is given by the Taylor expansion

$$T(t,\boldsymbol{x},\boldsymbol{y}) = S(t,\boldsymbol{y}) + \boldsymbol{p}(t,\boldsymbol{y})\cdot(\boldsymbol{x}-\boldsymbol{y}) + \frac{1}{2}(\boldsymbol{x}-\boldsymbol{y})^{\top}M(t,\boldsymbol{y})(\boldsymbol{x}-\boldsymbol{y}) + O(|\boldsymbol{x}-\boldsymbol{y}|^3), \tag{2.2}$$

in which $(\boldsymbol{x}-\boldsymbol{y})^{\top}$ is the transpose of $(\boldsymbol{x}-\boldsymbol{y})$. Here $S\in\mathbb{R}$, $\boldsymbol{p}\in\mathbb{R}^n$, $A\in\mathbb{C}$, $M\in\mathbb{C}^{n\times n}$. The imaginary part of M will be chosen so that (2.1) has a Gaussian beam profile. We call (2.1) the beam-shaped ansatz.

The difference from the WKB ansatz is that, in (2.1)–(2.2), a free parameter $\boldsymbol{y}$ is used to control the domain where the WKB analysis is applied. Actually, $\boldsymbol{y}$ plays the role of the beam center, chosen as

$$\frac{\mathrm{d}\boldsymbol{y}}{\mathrm{d}t} = \boldsymbol{p}(t,\boldsymbol{y}), \quad \boldsymbol{y}(0) = \boldsymbol{y}_0. \tag{2.3}$$

2.1. Formulation for the beam-shaped ansatz.   We first derive the formulation for the beam-shaped ansatz (2.1). Plugging (2.1) into (1.1) and equating the first two leading orders of ε, one obtains the following equations for T and A

$$\frac{\partial T}{\partial t} + \frac{\partial \boldsymbol{y}}{\partial t}\cdot\nabla_{\boldsymbol{y}}T + \frac{1}{2}|\nabla_{\boldsymbol{x}}T|^2 + V = 0, \tag{2.4}$$

$$\frac{\partial A}{\partial t} + \frac{\partial \boldsymbol{y}}{\partial t}\cdot\nabla_{\boldsymbol{y}}A + \frac{1}{2}(\triangle_{\boldsymbol{x}}T)A = 0. \tag{2.5}$$

Taking the first and second derivatives with respect to $\boldsymbol{x}$ in (2.4) gives

$$\frac{\partial(\nabla_{\boldsymbol{x}}T)}{\partial t} + \frac{\partial \boldsymbol{y}}{\partial t}\cdot\nabla_{\boldsymbol{y}\boldsymbol{x}}T + \nabla_{\boldsymbol{x}}T\cdot\nabla_{\boldsymbol{x}}^2 T + \nabla_{\boldsymbol{x}}V = 0, \tag{2.6}$$

$$\frac{\partial(\nabla_{\boldsymbol{x}}^2 T)}{\partial t} + \frac{\partial \boldsymbol{y}}{\partial t}\cdot\nabla_{\boldsymbol{y}\boldsymbol{x}\boldsymbol{x}}T + \left(\nabla_{\boldsymbol{x}}^2 T\right)^2 + \nabla_{\boldsymbol{x}}T\cdot\nabla_{\boldsymbol{x}}^3 T + \nabla_{\boldsymbol{x}}^2 V = 0. \tag{2.7}$$

Using (2.2) and evaluating (2.4)–(2.7) at $\boldsymbol{x}=\boldsymbol{y}$ yield (after ignoring the $O(|\boldsymbol{x}-\boldsymbol{y}|^3)$ term)

$$\frac{\partial S}{\partial t} + \frac{\partial \boldsymbol{y}}{\partial t}\cdot(\nabla_{\boldsymbol{y}}S - \boldsymbol{p}) + \frac{1}{2}|\boldsymbol{p}|^2 + V = 0, \tag{2.8}$$

$$\frac{\partial A}{\partial t} + \frac{\partial \boldsymbol{y}}{\partial t}\cdot\nabla_{\boldsymbol{y}}A + \frac{1}{2}\big(\mathrm{Tr}(M)\big)A = 0, \tag{2.9}$$

$$\frac{\partial \boldsymbol{p}}{\partial t} + \frac{\partial \boldsymbol{y}}{\partial t}\cdot(\nabla_{\boldsymbol{y}}\boldsymbol{p} - M) + \boldsymbol{p}\cdot M + \nabla_{\boldsymbol{y}}V = 0, \tag{2.10}$$

$$\frac{\partial M}{\partial t} + \frac{\partial \boldsymbol{y}}{\partial t}\cdot\nabla_{\boldsymbol{y}}M + M^2 + \nabla_{\boldsymbol{y}}^2 V = 0, \tag{2.11}$$

where $\mathrm{Tr}(M)$ is the trace of the matrix M.

Considering the $\boldsymbol{y}$-trajectory given by (2.3), then (2.8)-(2.11) can be written as a set of ODEs:

$$\frac{\mathrm{d}\boldsymbol{y}}{\mathrm{d}t} = \boldsymbol{p}, \tag{2.12}$$

$$\frac{\mathrm{d}\boldsymbol{p}}{\mathrm{d}t} = -\nabla_{\boldsymbol{y}}V, \tag{2.13}$$

$$\frac{\mathrm{d}M}{\mathrm{d}t} = -M^2 - \nabla_{\boldsymbol{y}}^2 V, \tag{2.14}$$

$$\frac{\mathrm{d}S}{\mathrm{d}t} = \frac{1}{2}|\boldsymbol{p}|^2 - V, \tag{2.15}$$

$$\frac{\mathrm{d}A}{\mathrm{d}t} = -\frac{1}{2}\big(\mathrm{Tr}(M)\big)A. \tag{2.16}$$

Here $\boldsymbol{y} = \boldsymbol{y}(t, \boldsymbol{y}_0)$, $\boldsymbol{p} = \boldsymbol{p}(t, \boldsymbol{y}(t, \boldsymbol{y}_0))$, $V = V(\boldsymbol{y}(t, \boldsymbol{y}_0))$, $M = M(t, \boldsymbol{y}(t, \boldsymbol{y}_0))$, and $S = S(t, \boldsymbol{y}(t, \boldsymbol{y}_0))$, $A = A(t, \boldsymbol{y}(t, \boldsymbol{y}_0))$.

Equations (2.12)–(2.16) are the Lagrangian formulation of the Gaussian beam method. (2.12)-(2.13) are called the ray-tracing equations, and (2.14) is a Riccati equation for the Hessian M, which will be solved by the dynamic first order system of ray tracing equations (2.17).

We summarize some properties of these ODEs in Theorem 2.1. The results and proofs of Parts 1, 2 and 3 essentially follow those in [29].

THEOREM 2.1. *Let $P(t, \boldsymbol{y}(t, \boldsymbol{y}_0))$ and $R(t, \boldsymbol{y}(t, \boldsymbol{y}_0))$ be the (global) solutions of the equations*

$$\frac{\mathrm{d}P}{\mathrm{d}t} = R, \quad \frac{\mathrm{d}R}{\mathrm{d}t} = -(\nabla_{\boldsymbol{y}}^2 V)P, \tag{2.17}$$

with initial conditions

$$P(0, \boldsymbol{y}_0) = I, \, R(0, \boldsymbol{y}_0) = M(0, \boldsymbol{y}_0), \tag{2.18}$$

where matrix I is the identity matrix and $\mathrm{Im}(M(0, \boldsymbol{y}_0))$ is positive definite. Assume $M(0, \boldsymbol{y}_0)$ is symmetric. Then for each initial position $\boldsymbol{y}_0$, we have the following.

1. *$P(t, \boldsymbol{y}(t, \boldsymbol{y}_0))$ is invertible for all $t > 0$.*

2. *The solution to equation (2.14) is given by*

$$M(t, \boldsymbol{y}(t, \boldsymbol{y}_0)) = R(t, \boldsymbol{y}(t, \boldsymbol{y}_0))P^{-1}(t, \boldsymbol{y}(t, \boldsymbol{y}_0)). \tag{2.19}$$

3. *$M(t, \boldsymbol{y}(t, \boldsymbol{y}_0))$ is symmetric and $\mathrm{Im}(M(t, \boldsymbol{y}(t, \boldsymbol{y}_0)))$ is positive definite for all $t > 0$.*

4. *Not only is the Hamiltonian $V + \frac{1}{2}|\boldsymbol{p}|^2$ conserved along the $\boldsymbol{y}$-trajectory, another quantity $A^2 \det P$ is also conserved, which means $A(t, \boldsymbol{y}(t, \boldsymbol{y}_0))$ can also be computed by*

$$A(t, \boldsymbol{y}(t, \boldsymbol{y}_0)) = \big[(\det P(t, \boldsymbol{y}(t, \boldsymbol{y}_0)))^{-1} A^2(0, \boldsymbol{y}_0)\big]^{1/2}, \tag{2.20}$$

where the square root is taken as the principal value.

Proof. Since $\boldsymbol{y}(t, \boldsymbol{y}_0)$ is not involved in the proof, we drop it for convenience and simply write $M(t, \boldsymbol{y}(t, \boldsymbol{y}_0))$, $A(t, \boldsymbol{y}(t, \boldsymbol{y}_0))$, $P(t, \boldsymbol{y}(t, \boldsymbol{y}_0))$, and $R(t, \boldsymbol{y}(t, \boldsymbol{y}_0))$ as $M(t)$, $A(t)$, $P(t)$, and $R(t)$, respectively.

(1) For any vector $\boldsymbol{\eta} \in \mathbb{C}^n$, by (2.17), $\boldsymbol{z}_1 = P(t)\boldsymbol{\eta}$ and $\boldsymbol{z}_2 = R(t)\boldsymbol{\eta}$ satisfy

$$\frac{\mathrm{d}\boldsymbol{z}_1}{\mathrm{d}t} = \boldsymbol{z}_2, \quad \frac{\mathrm{d}\boldsymbol{z}_2}{\mathrm{d}t} = -(\nabla_{\boldsymbol{y}}^2 V)\boldsymbol{z}_1. \tag{2.21}$$

Define

$$\sigma(P, R, \boldsymbol{\eta}) = \overline{\boldsymbol{z}}_1 \cdot \boldsymbol{z}_2 - \boldsymbol{z}_1 \cdot \overline{\boldsymbol{z}}_2. \tag{2.22}$$

Note that $\nabla_{\boldsymbol{y}}^2 V$ is real and symmetric. Then by differentiating (2.22) with respect to t and using (2.21), one has

$$\begin{aligned}
\frac{\mathrm{d}}{\mathrm{d}t}\sigma(P, R, \boldsymbol{\eta}) &= \frac{\mathrm{d}\overline{\boldsymbol{z}}_1}{\mathrm{d}t} \cdot \boldsymbol{z}_2 + \overline{\boldsymbol{z}}_1 \cdot \frac{\mathrm{d}\boldsymbol{z}_2}{\mathrm{d}t} - \frac{\mathrm{d}\boldsymbol{z}_1}{\mathrm{d}t} \cdot \overline{\boldsymbol{z}}_2 - \boldsymbol{z}_1 \cdot \frac{\mathrm{d}\overline{\boldsymbol{z}}_2}{\mathrm{d}t} \\
&= \overline{\boldsymbol{z}}_2 \cdot \boldsymbol{z}_2 + \overline{\boldsymbol{z}}_1 \cdot \big((-\nabla_{\boldsymbol{y}}^2 V)\boldsymbol{z}_1\big) - \boldsymbol{z}_2 \cdot \overline{\boldsymbol{z}}_2 - \boldsymbol{z}_1 \cdot \big((-\nabla_{\boldsymbol{y}}^2 V)\overline{\boldsymbol{z}}_1\big) \\
&= 0.
\end{aligned}$$

Assume that $P(t)$ is singular at $t = t_0$. Then there exists a non-zero vector $\boldsymbol{l} \in \mathbb{C}^n$ such that $P(t_0)\boldsymbol{l} = 0$. So, we have

$$\begin{aligned}
0 &= \overline{P(t_0)\boldsymbol{l}} \cdot R(t_0)\boldsymbol{l} - P(t_0)\boldsymbol{l} \cdot \overline{R(t_0)\boldsymbol{l}} \\
&= \sigma(P(t_0), R(t_0), \boldsymbol{l}) = \sigma(P(0), R(0), \boldsymbol{l}) \\
&= \overline{P(0)\boldsymbol{l}} \cdot R(0)\boldsymbol{l} - P(0)\boldsymbol{l} \cdot \overline{R(0)\boldsymbol{l}} \\
&= \overline{\boldsymbol{l}} \cdot M(0)\boldsymbol{l} - \boldsymbol{l} \cdot \overline{M(0)\boldsymbol{l}} = 2i\overline{\boldsymbol{l}} \cdot \mathrm{Im}[M(0)]\boldsymbol{l},
\end{aligned}$$

which is a contradiction since $\mathrm{Im}[M(0)]$ is positive definite and $\boldsymbol{l}_0$ is non-zero. In the last identity we used the symmetry of $M(0)$.

This proves the invertibility of $P(t)$.

(2) Let $M = RP^{-1}$. Using (2.17), one obtains

$$\begin{aligned}
\frac{\mathrm{d}M}{\mathrm{d}t} + M^2 + \nabla_{\boldsymbol{y}}^2 V &= \frac{\mathrm{d}R}{\mathrm{d}t}P^{-1} + R\frac{\mathrm{d}P^{-1}}{\mathrm{d}t} + RP^{-1}RP^{-1} + \nabla_{\boldsymbol{y}}^2 V \\
&= -(\nabla_{\boldsymbol{y}}^2 V)PP^{-1} - RP^{-1}\frac{\mathrm{d}P}{\mathrm{d}t}P^{-1} + RP^{-1}RP^{-1} + \nabla_{\boldsymbol{y}}^2 V \\
&= -RP^{-1}RP^{-1} + RP^{-1}RP^{-1} = 0.
\end{aligned}$$

Thus M satisfies (2.14).

(3) First, since both $M(t)$ and its transpose $M^\top(t)$ satisfy the same equation (2.14), the uniqueness (for example, Theorem 1 in [7]) implies that $M(t) = M^\top(t)$ for all $t > 0$, when the initial condition $M(0)$ is symmetric.

Since we already proved that $P(t)$ is invertible, $\forall \boldsymbol{l}' \in \mathbb{C}^n$ there exists an $\boldsymbol{l}$ that satisfies $\boldsymbol{l}' = P(t)\boldsymbol{l}$. Then

$$\begin{aligned}
2i\overline{\boldsymbol{l}'} \cdot \mathrm{Im}[M(t)]\boldsymbol{l}' &= 2i\overline{P(t)\boldsymbol{l}} \cdot \mathrm{Im}[M(t)]P(t)\boldsymbol{l} \\
&= \overline{P(t)\boldsymbol{l}} \cdot M(t)P(t)\boldsymbol{l} - P(t)\boldsymbol{l} \cdot \overline{M(t)P(t)\boldsymbol{l}} \\
&= \overline{P(t)\boldsymbol{l}} \cdot R(t)\boldsymbol{l} - P(t)\boldsymbol{l} \cdot \overline{R(t)\boldsymbol{l}} \\
&= \sigma(P(t), R(t), \boldsymbol{l}) = \sigma(P(0), R(0), \boldsymbol{l}) \\
&= \overline{P(0)\boldsymbol{l}} \cdot R(0)\boldsymbol{l} - P(0)\boldsymbol{l} \cdot \overline{R(0)\boldsymbol{l}} \\
&= \overline{P(0)\boldsymbol{l}} \cdot M(0)P(0)\boldsymbol{l} - P(0)\boldsymbol{l} \cdot \overline{M(0)P(0)\boldsymbol{l}} \\
&= 2i\overline{\boldsymbol{l}} \cdot \mathrm{Im}[M(0)]\boldsymbol{l}.
\end{aligned}$$

The second and last identities are obtained by the symmetries of $M(t)$ and $M(0)$. Because $\text{Im}[M(0)]$ is positive definite, $\text{Im}[M(t)]$ is also positive definite.

(4) Along the $\boldsymbol{y}$-trajectory,

$$
\begin{aligned}
\frac{\mathrm{d}}{\mathrm{d}t}\left(A^2 \det P\right) &= 2A\frac{\mathrm{d}A}{\mathrm{d}t}\det P + A^2\frac{\mathrm{d}(\det P)}{\mathrm{d}t} \\
&= -2A\left[\frac{1}{2}\left(\text{Tr}(M)\right)A\right]\det P + A^2\text{Tr}\left(P^{-1}\frac{\mathrm{d}P}{\mathrm{d}t}\right)\det P \\
&= -A^2\text{Tr}\left(RP^{-1}\right)\det P + A^2\text{Tr}\left(P^{-1}R\right)\det P = 0.
\end{aligned}
$$

Hence $A^2 \det P$ is conserved. $\qquad\square$

2.2. The Lagrangian Gaussian beam summation. In this subsection, we introduce the Lagrangian Gaussian beam summation formula (for example [12]). The approximation of the WKB initial data (1.2) is shown in the next theorem proved by Tanushev in [30]. Note that the regularities of the initial conditions are modified to be specific here.

THEOREM 2.2. *Let $A_0 \in C^1(\mathbb{R}^n)\cap L^2(\mathbb{R}^n)$ and $S_0 \in C^3(\mathbb{R}^n)$, and define*

$$
\begin{aligned}
\Psi_0^\varepsilon(\boldsymbol{x}) &= A_0(\boldsymbol{x})e^{iS_0(\boldsymbol{x})/\varepsilon}, \\
\varphi_0^\varepsilon(\boldsymbol{x},\boldsymbol{y}_0) &= A_0(\boldsymbol{y}_0)e^{iT_0(\boldsymbol{x},\boldsymbol{y}_0)/\varepsilon},
\end{aligned}
$$

where

$$
\begin{aligned}
T_0(\boldsymbol{x},\boldsymbol{y}_0) &= T_{\alpha 0}(\boldsymbol{y}_0) + T_{\beta 0}\cdot(\boldsymbol{x}-\boldsymbol{y}_0) + \frac{1}{2}(\boldsymbol{x}-\boldsymbol{y}_0)^\top T_{\gamma 0}(\boldsymbol{x}-\boldsymbol{y}_0), \\
T_{\alpha 0}(\boldsymbol{y}_0) &= S_0(\boldsymbol{y}_0), \quad T_{\beta 0}(\boldsymbol{y}_0) = \nabla_{\boldsymbol{x}}S_0(\boldsymbol{y}_0), \quad T_{\gamma 0}(\boldsymbol{y}_0) = \nabla_{\boldsymbol{x}}^2 S_0(\boldsymbol{y}_0) + iI.
\end{aligned}
$$

Then

$$
\left\|\int_{\mathbb{R}^n}\left(\frac{1}{2\pi\varepsilon}\right)^{\frac{n}{2}}r_\theta(\boldsymbol{x}-\boldsymbol{y}_0)\varphi_0^\varepsilon(\boldsymbol{x},\boldsymbol{y}_0)\mathrm{d}\boldsymbol{y}_0 - \Psi_0^\varepsilon(\boldsymbol{x})\right\|_{L^2} \leq C\varepsilon^{\frac{1}{2}},
$$

where $r_\theta \in C_0^\infty(\mathbb{R}^n)$, $r_\theta \geq 0$ is a truncation function with $r_\theta \equiv 1$ in a ball of radius $\theta > 0$ about the origin, and C is a constant related to θ.

By Theorem 2.2 we specify the initial data for (2.12)–(2.16) as

$$
\begin{aligned}
\boldsymbol{y}(0,\boldsymbol{y}_0) &= \boldsymbol{y}_0, & (2.23) \\
\boldsymbol{p}(0,\boldsymbol{y}_0) &= \nabla_{\boldsymbol{x}}S_0(\boldsymbol{y}_0), & (2.24) \\
M(0,\boldsymbol{y}_0) &= \nabla_{\boldsymbol{x}}^2 S_0(\boldsymbol{y}_0) + iI, & (2.25) \\
S(0,\boldsymbol{y}_0) &= S_0(\boldsymbol{y}_0), & (2.26) \\
A(0,\boldsymbol{y}_0) &= A_0(\boldsymbol{y}_0). & (2.27)
\end{aligned}
$$

Then the Gaussian beam summation solution which approximates the Schrödinger Equation (1.1) is constructed as:

$$
\Phi_{la}^\varepsilon(t,\boldsymbol{x}) = \int_{\mathbb{R}^n}\left(\frac{1}{2\pi\varepsilon}\right)^{\frac{n}{2}}r_\theta(\boldsymbol{x}-\boldsymbol{y}(t,\boldsymbol{y}_0))\varphi_{la}^\varepsilon(t,\boldsymbol{x},\boldsymbol{y}_0)\mathrm{d}\boldsymbol{y}_0. \qquad (2.28)
$$

The discrete form of (2.28) in a bounded domain is given by

$$\Phi_{la}^{\varepsilon}(t,\boldsymbol{x}) = \sum_{j=1}^{N_{\boldsymbol{y}_0}} \left(\frac{1}{2\pi\varepsilon}\right)^{\frac{n}{2}} r_\theta(\boldsymbol{x} - \boldsymbol{y}(t,\boldsymbol{y}_0^j)) \varphi_{la}^{\varepsilon}(t,\boldsymbol{x},\boldsymbol{y}_0^j) \Delta\boldsymbol{y}_0, \qquad (2.29)$$

where $\boldsymbol{y}_0^j$ are the equidistant mesh points, and $N_{\boldsymbol{y}_0}$ is the number of the beams initially centered at $\boldsymbol{y}_0^j$.

Note that r_θ works as a cut-off function, and the cut-off error becomes large when the truncation parameter θ is taken too small. On the other hand, a large θ, for wide beams, makes the Taylor expansion error large. As far as we know, it is still an open question how large θ should be chosen when the beams spread. However, for narrow beams one could take fairly large θ, which makes the cut-off error almost zero. For example, a one-dimensional constant solution could be approximated by

$$1 = \int_{\mathbb{R}} \frac{1}{\sqrt{2\pi\varepsilon}} \exp\left(\frac{-(x-y_0)^2}{2\varepsilon}\right) dy_0 \approx \sum_j \frac{\Delta y_0}{\sqrt{2\pi\varepsilon}} \exp\left(\frac{-(x-y_0^j)^2}{2\varepsilon}\right),$$

in which $r_\theta \equiv 1$.

3. The Eulerian formulation

In the last few years, the level set method has been developed to compute the multi-valued solution of (1.7)–(1.8) which gives the correct semiclassical limit of the Schrödinger solution [16, 5, 15] *away from the caustics*. The idea is to build the velocity $\boldsymbol{u} = \nabla_{\boldsymbol{y}} S$ into the intersection of zero level sets of phase-space functions $\phi_j(t,\boldsymbol{y},\boldsymbol{\xi}), j = 1,\cdots,n$, i.e.,

$$\phi_j(t,\boldsymbol{y},\boldsymbol{\xi}) = 0, \quad \text{at} \quad \boldsymbol{\xi} = \boldsymbol{u}(t,\boldsymbol{y}), \quad j = 1,\cdots,n. \qquad (3.1)$$

If we define $\boldsymbol{\phi} = (\phi_1,\cdots,\phi_n)$, then by differentiating (3.1) with respect to $\boldsymbol{y}$ for each j, the Hessian $\nabla_{\boldsymbol{y}}\boldsymbol{u}$ satisfies

$$\nabla_{\boldsymbol{y}}^2 S = \nabla_{\boldsymbol{y}}\boldsymbol{u} = -\nabla_{\boldsymbol{y}}\boldsymbol{\phi}(\nabla_{\boldsymbol{\xi}}\boldsymbol{\phi})^{-1}. \qquad (3.2)$$

Comparing (3.2) with (2.19), we conjecture that

$$R = -\nabla_{\boldsymbol{y}}\boldsymbol{\phi}, \quad P = \nabla_{\boldsymbol{\xi}}\boldsymbol{\phi}. \qquad (3.3)$$

Note that this conjecture does not violate the symmetry of the Hessian $\nabla_{\boldsymbol{y}}\boldsymbol{u}$ by the second and third parts of Theorem 2.1. Moreover, it also implies the divergence-free condition

$$\nabla_{\boldsymbol{\xi}}R + \nabla_{\boldsymbol{y}}P = 0, \qquad (3.4)$$

which actually holds initially (2.18).

In this section, we first review the level set formulations developed in [15, 16, 19] for geometrical optics, and then prove that the conjecture (3.3) is true under an appropriate initial condition for $\boldsymbol{\phi}$. We then describe the level set algorithm for the Eulerian Gaussian beam method and the construction of the wave function for the Schrödinger equation. Although our new formulations are consistent with the Eulerian Gaussian beam method constructed in [19] for the Helmholtz equations, by making use of observation (3.3) we introduce a much simpler and efficient numerical method than [19].

3.1. Verification of (3.3)   Define the linear Liouville operator as

$$\mathcal{L} = \partial_t + \boldsymbol{\xi} \cdot \nabla_{\boldsymbol{y}} - \nabla_{\boldsymbol{y}} V \cdot \nabla_{\boldsymbol{\xi}}.$$

As shown in [15, 16], the level set equations for the velocity, phase and amplitude are given by

$$\mathcal{L}\boldsymbol{\phi} = 0, \tag{3.5}$$

$$\mathcal{L}S = \frac{1}{2}|\boldsymbol{\xi}|^2 - V, \tag{3.6}$$

$$\mathcal{L}A = \frac{1}{2}\mathrm{Tr}\left((\nabla_{\boldsymbol{\xi}}\boldsymbol{\phi})^{-1}\nabla_{\boldsymbol{y}}\boldsymbol{\phi}\right)A. \tag{3.7}$$

If one introduces the new quantity ([15])

$$f(t,\boldsymbol{y},\boldsymbol{\xi}) = A^2(t,\boldsymbol{y},\boldsymbol{\xi})\det(\nabla_{\boldsymbol{\xi}}\boldsymbol{\phi}), \tag{3.8}$$

then $f(t,\boldsymbol{y},\boldsymbol{\xi})$ satisfies the Liouville equation

$$\mathcal{L}f = 0. \tag{3.9}$$

For the Gaussian beam method in [19], two more inhomogeneous Liouville equations, which are the Eulerian formula of (2.17) for P and R, were introduced to construct the Hessian matrix

$$\mathcal{L}R = -(\nabla_{\boldsymbol{y}}^2 V)P, \tag{3.10}$$
$$\mathcal{L}P = R. \tag{3.11}$$

Note that the equations (3.5)–(3.9) are *real*, while (3.10)–(3.11) are *complex* and consist of $2n^2$ equations.

By taking the gradient of equation (3.5) with respect to $\boldsymbol{y}$ and $\boldsymbol{\xi}$ separately, we have

$$\mathcal{L}(\nabla_{\boldsymbol{y}}\boldsymbol{\phi}) = \nabla_{\boldsymbol{y}}^2 V \nabla_{\boldsymbol{\xi}}\boldsymbol{\phi}, \tag{3.12}$$
$$\mathcal{L}(\nabla_{\boldsymbol{\xi}}\boldsymbol{\phi}) = -\nabla_{\boldsymbol{y}}\boldsymbol{\phi}. \tag{3.13}$$

Comparing (3.10)–(3.11) with (3.12)–(3.13), we observe that $-\nabla_{\boldsymbol{y}}\boldsymbol{\phi}$ and $\nabla_{\boldsymbol{\xi}}\boldsymbol{\phi}$ satisfy the same equations as R and P. Since the Liouville equations are linear, the conjecture (3.3) is true by letting $\boldsymbol{\phi}$ be *complex* and by enforcing that $-\nabla_{\boldsymbol{y}}\boldsymbol{\phi}, \nabla_{\boldsymbol{\xi}}\boldsymbol{\phi}$ have the same initial conditions as R and P respectively.

From (2.18) and (2.25), this suggests the following initial condition for $\boldsymbol{\phi}$:

$$\boldsymbol{\phi}_0(\boldsymbol{y},\boldsymbol{\xi}) = -i\boldsymbol{y} + (\boldsymbol{\xi} - \nabla_{\boldsymbol{y}}S_0). \tag{3.14}$$

With this observation, we can now solve (3.5) for *complex* $\boldsymbol{\phi}$, with initial data (3.14). Then the Hessian M is constructed by

$$M = -\nabla_{\boldsymbol{y}}\boldsymbol{\phi}(\nabla_{\boldsymbol{\xi}}\boldsymbol{\phi})^{-1}, \tag{3.15}$$

where velocity $\boldsymbol{u} = -\nabla_{\boldsymbol{y}}S$ is given by the intersection of the zero-level contours of the *real* part of $\boldsymbol{\phi}$, i.e., for each component ϕ_j,

$$\mathrm{Re}[\phi_j(t,\boldsymbol{y},\boldsymbol{\xi})] = 0, \quad \text{at} \quad \boldsymbol{\xi} = \boldsymbol{u}(t,\boldsymbol{y}) = \nabla_{\boldsymbol{y}}S. \tag{3.16}$$

Note that to compute $\boldsymbol{u}, S$ and M we just need to solve n complex-valued *homogeneous* Liouville Equation (3.5), while in the formulation of [19], one needs to solve n real-valued homogeneous Liouville Equation (3.5) and $2n^2$ complex-valued *inhomogeneous* Liouville equations (3.10) and (3.11). Our new formulation has a computational complexity comparable to that of the level set methods for geometrical optics [15, 17]. The only difference here is that (3.5) is complex-valued while in the geometrical optics computation one solves the real part.

3.2. The level set algorithm.   In this subsection, we give the implementation details of the new level set method. We will also prove its validity at caustics.

- Step 1. Solve (3.5) for *complex* ϕ, with initial condition (3.14), then obtain the velocity $\boldsymbol{u}$ by the intersection of the zero-level sets of $\mathrm{Re}\phi_j$, $j = 1, \cdots, n$.
- Step 2. Use $-\nabla_{\boldsymbol{y}}\phi$ and $\nabla_{\boldsymbol{\xi}}\phi$ to construct the Hessian matrix by (3.15) (note these quantities actually are already available from the first step when one discretizes the Liouville equation for ϕ).
- Step 3. One can integrate the velocity $\boldsymbol{u}$ along the zero-level sets ([10, 17]) to get the phase S. The idea is to do numerical integration following each branch of the velocity. The integration constants are obtained by both the boundary condition and the fact that the multivalued phase is continuous when it passes from one branch to the other. For example, if we consider a bounded domain $[a, b]$ in one space dimension, the phase function is given by

$$S(t, x) = -V(a)t - \frac{1}{2}\int_0^t u^2(\tau, a)\mathrm{d}\tau + \int_a^x u(t, s)\mathrm{d}s + S(0, a). \qquad (3.17)$$

Because $\int_a^x u(t, s)ds$ is the only term in (3.17) which affects the quadratic physical observables for fixed time t, one could take

$$S(t, x) = \int_a^x u(t, s)\mathrm{d}s \qquad (3.18)$$

as the phase value in the numerical simulations of (1.3)-(1.5). For more details and in higher dimensions, see [17]. (One could also solve (3.6) directly.)

- Step 4. Solve (3.9) with the initial condition

$$f_0(\boldsymbol{y}, \boldsymbol{\xi}) = A_0^2(\boldsymbol{y}, \boldsymbol{\xi}).$$

The amplitude A is given by

$$A = (\det(\nabla_{\boldsymbol{\xi}}\phi)^{-1}f)^{1/2}, \qquad (3.19)$$

in which the square root is taken as the principal value.

REMARK 3.1. All of the functions in Steps 2–4 only need to be solved locally around the zero-level sets of $\mathrm{Re}\phi_j$, $j = 1, \cdots, n$. Namely, the entire algorithm can be implemented using the local level set methods [26, 27], thus the computational cost for mesh size Δy is $O((\Delta y)^{-n}\ln(\Delta y)^{-1})$, about the same as the local level set methods for geometrical optics computations [15, 17].

The well-definedness of (3.15) and (3.19) is justified by the following theorem, which is the Eulerian version of Theorem 2.1.

THEOREM 3.2. *Let $\phi = \phi(t, \boldsymbol{y}, \boldsymbol{\xi}) \in \mathbb{C}$ be the solution of (3.5) with initial data (3.14). Then we have the following properties:*

1. $\nabla_{\boldsymbol{\xi}}\phi$ is non-degenerate for all $t>0$.
2. $Im\left(-\nabla_{\boldsymbol{y}}\phi(\nabla_{\boldsymbol{\xi}}\phi)^{-1}\right)$ is positive definite for all $t>0$, $\boldsymbol{y},\boldsymbol{\xi}\in\mathbb{R}^n$.

Proof. (1) For $\forall\boldsymbol{\eta}\in\mathbb{C}^n$, by using (3.12)-(3.13) we have

$$\mathcal{L}\left(\overline{(\nabla_{\boldsymbol{\xi}}\phi)\boldsymbol{\eta}}\cdot(\nabla_{\boldsymbol{y}}\phi)\boldsymbol{\eta}-(\nabla_{\boldsymbol{\xi}}\phi)\boldsymbol{\eta}\cdot\overline{(\nabla_{\boldsymbol{y}}\phi)\boldsymbol{\eta}}\right)$$

$$=\mathcal{L}\left(\overline{(\nabla_{\boldsymbol{\xi}}\phi)\boldsymbol{\eta}}\right)\cdot(\nabla_{\boldsymbol{y}}\phi)\boldsymbol{\eta}+\overline{(\nabla_{\boldsymbol{\xi}}\phi)\boldsymbol{\eta}}\cdot\mathcal{L}((\nabla_{\boldsymbol{y}}\phi)\boldsymbol{\eta})$$
$$-\mathcal{L}((\nabla_{\boldsymbol{\xi}}\phi)\boldsymbol{\eta})\cdot\overline{(\nabla_{\boldsymbol{y}}\phi)\boldsymbol{\eta}}-(\nabla_{\boldsymbol{\xi}}\phi)\boldsymbol{\eta}\cdot\mathcal{L}\left(\overline{(\nabla_{\boldsymbol{y}}\phi)\boldsymbol{\eta}}\right)$$

$$=-\overline{(\nabla_{\boldsymbol{y}}\phi)\boldsymbol{\eta}}\cdot(\nabla_{\boldsymbol{y}}\phi)\boldsymbol{\eta}+\overline{(\nabla_{\boldsymbol{\xi}}\phi)\boldsymbol{\eta}}\cdot\left((\nabla_{\boldsymbol{y}}^2V\cdot\nabla_{\boldsymbol{\xi}}\phi)\boldsymbol{\eta}\right)$$
$$+(\nabla_{\boldsymbol{y}}\phi)\boldsymbol{\eta}\cdot\overline{(\nabla_{\boldsymbol{y}}\phi)\boldsymbol{\eta}}-(\nabla_{\boldsymbol{\xi}}\phi)\boldsymbol{\eta}\cdot\overline{\left((\nabla_{\boldsymbol{y}}^2V\cdot\nabla_{\boldsymbol{\xi}}\phi)\boldsymbol{\eta}\right)}$$

$$=0.$$

The last equality is true because $\nabla_{\boldsymbol{y}}^2V$ is symmetric and real.

If $\nabla_{\boldsymbol{\xi}}\phi$ is singular at $(t_2,\boldsymbol{y}_2,\boldsymbol{\xi}_2)$, there exists a non-zero $\boldsymbol{l}\in\mathbb{C}^n$ such that $(\nabla_{\boldsymbol{\xi}}\phi)\boldsymbol{l}\big|_{(t_2,\boldsymbol{y}_2,\boldsymbol{\xi}_2)}=0$. Then we have

$$\left(\overline{(\nabla_{\boldsymbol{\xi}}\phi)\boldsymbol{l}}\cdot(\nabla_{\boldsymbol{y}}\phi)\boldsymbol{l}-(\nabla_{\boldsymbol{\xi}}\phi)\boldsymbol{l}\cdot\overline{(\nabla_{\boldsymbol{y}}\phi)\boldsymbol{l}}\right)\Big|_{(t_2,\boldsymbol{y}_2,\boldsymbol{\xi}_2)}=0.$$

Since $\mathcal{L}\left(\overline{(\nabla_{\boldsymbol{\xi}}\phi)\boldsymbol{l}}\cdot(\nabla_{\boldsymbol{y}}\phi)\boldsymbol{l}-(\nabla_{\boldsymbol{\xi}}\phi)\boldsymbol{l}\cdot\overline{(\nabla_{\boldsymbol{y}}\phi)\boldsymbol{l}}\right)=0$, there exists $(0,\boldsymbol{y}_1,\boldsymbol{\xi}_1)$ that connects $(t_2,\boldsymbol{y}_2,\boldsymbol{\xi}_2)$ by a characteristic such that

$$\left(\overline{(\nabla_{\boldsymbol{\xi}}\phi)\boldsymbol{l}}\cdot(\nabla_{\boldsymbol{y}}\phi)\boldsymbol{l}-(\nabla_{\boldsymbol{\xi}}\phi)\boldsymbol{l}\cdot\overline{(\nabla_{\boldsymbol{y}}\phi)\boldsymbol{l}}\right)\Big|_{(0,\boldsymbol{y}_1,\boldsymbol{\xi}_1)}$$
$$=\left(\overline{(\nabla_{\boldsymbol{\xi}}\phi)\boldsymbol{l}}\cdot(\nabla_{\boldsymbol{y}}\phi)\boldsymbol{l}-(\nabla_{\boldsymbol{\xi}}\phi)\boldsymbol{l}\cdot\overline{(\nabla_{\boldsymbol{y}}\phi)\boldsymbol{l}}\right)\Big|_{(t_2,\boldsymbol{y}_2,\boldsymbol{\xi}_2)}$$
$$=0.$$

This implies, by taking account of the initial condition (3.14),

$$-2i\overline{\boldsymbol{l}}\cdot\boldsymbol{l}=0.$$

This is a contradiction, which proves $\nabla_{\boldsymbol{\xi}}\phi$ is not degenerate for all $t>0$.

(2) Since we already proved that $\nabla_{\boldsymbol{\xi}}\phi$ is non-degenerate, $\forall\boldsymbol{l}'\in\mathbb{C}^n$ there exists an $\boldsymbol{l}$ that satisfies $\boldsymbol{l}'=(\nabla_{\boldsymbol{\xi}}\phi)\boldsymbol{l}$. Note that $-\nabla_{\boldsymbol{y}}\phi(\nabla_{\boldsymbol{\xi}}\phi)^{-1}$ is symmetric from (3.2), then we have

$$2i\overline{\boldsymbol{l}'}\cdot Im\left(-\nabla_{\boldsymbol{y}}\phi(\nabla_{\boldsymbol{\xi}}\phi)^{-1}\right)\big|_{(t_2,\boldsymbol{y}_2,\boldsymbol{\xi}_2)}\boldsymbol{l}'$$
$$=2i\left(\overline{(\nabla_{\boldsymbol{\xi}}\phi)\boldsymbol{l}}\cdot Im\left(-\nabla_{\boldsymbol{y}}\phi(\nabla_{\boldsymbol{\xi}}\phi)^{-1}\right)(\nabla_{\boldsymbol{\xi}}\phi)\boldsymbol{l}\right)\Big|_{(t_2,\boldsymbol{y}_2,\boldsymbol{\xi}_2)}$$
$$=-\left(\overline{(\nabla_{\boldsymbol{\xi}}\phi)\boldsymbol{l}}\cdot(\nabla_{\boldsymbol{y}}\phi)\boldsymbol{l}-(\nabla_{\boldsymbol{\xi}}\phi)\boldsymbol{l}\cdot\overline{(\nabla_{\boldsymbol{y}}\phi)\boldsymbol{l}}\right)\Big|_{(t_2,\boldsymbol{y}_2,\boldsymbol{\xi}_2)}$$
$$=-\left(\overline{(\nabla_{\boldsymbol{\xi}}\phi)\boldsymbol{l}}\cdot(\nabla_{\boldsymbol{y}}\phi)\boldsymbol{l}-(\nabla_{\boldsymbol{\xi}}\phi)\boldsymbol{l}\cdot\overline{(\nabla_{\boldsymbol{y}}\phi)\boldsymbol{l}}\right)\Big|_{(0,\boldsymbol{y}_1,\boldsymbol{\xi}_1)}$$
$$=2i\overline{\boldsymbol{l}}\cdot\boldsymbol{l},$$

which implies that $\operatorname{Im}\left(-\nabla_{\boldsymbol{y}}\phi(\nabla_{\boldsymbol{\xi}}\phi)^{-1}\right)$ is positive definite.   □

REMARK 3.3. Although $\det\left(\operatorname{Re}[\nabla_{\boldsymbol{\xi}}\phi]\right)=0$ at caustics, the complexified ϕ makes $\nabla_{\boldsymbol{\xi}}\phi$ non-degenerate, and the amplitude A, defined in (3.19), does not blow-up at caustics!

So far we have obtained the phase S, the velocity $\boldsymbol{u}$, the Hessian M, and the amplitude A. We show how to construct the wave function from these quantities in the next subsection.

3.3. The Eulerian Gaussian beam summation.   Define

$$\varphi_{eu}^{\varepsilon}(t,\boldsymbol{x},\boldsymbol{y},\boldsymbol{\xi})=A(t,\boldsymbol{y},\boldsymbol{\xi})e^{iT(t,\boldsymbol{x},\boldsymbol{y},\boldsymbol{\xi})/\varepsilon}, \tag{3.20}$$

where

$$T(t,\boldsymbol{x},\boldsymbol{y},\boldsymbol{\xi})=S(t,\boldsymbol{y},\boldsymbol{\xi})+\boldsymbol{\xi}\cdot(\boldsymbol{x}-\boldsymbol{y})+\frac{1}{2}(\boldsymbol{x}-\boldsymbol{y})^{\top}M(t,\boldsymbol{y},\boldsymbol{\xi})(\boldsymbol{x}-\boldsymbol{y}).$$

Then the wave function is constructed via the following Eulerian Gaussian beam summation formula:

$$\Phi_{eu}^{\varepsilon}(t,\boldsymbol{x})=\int_{\mathbb{R}^n}\int_{\mathbb{R}^n}\left(\frac{1}{2\pi\varepsilon}\right)^{\frac{n}{2}}r_{\theta}(\boldsymbol{x}-\boldsymbol{y})\varphi_{eu}^{\varepsilon}(t,\boldsymbol{x},\boldsymbol{y},\boldsymbol{\xi})\Pi_{j=1}^{n}\delta(\operatorname{Re}[\phi_j])d\boldsymbol{\xi}d\boldsymbol{y}, \tag{3.21}$$

in which $r_{\theta}\in C_0^{\infty}(\mathbb{R}^n)$, $r_{\theta}\geq 0$ is a truncation function with $r_{\theta}\equiv 1$ in a ball of radius $\theta>0$ about the origin and δ is the Dirac delta function. The choice of r_{θ} is the same as the one in the Lagrangian formulation.

We show in the Appendix that (3.21) is consistent to the Lagrangian summation formula (2.28). (3.21) could be evaluated as a single integral about $\boldsymbol{y}$. Since the velocity becomes multivalued after caustic formation, we denote $\boldsymbol{u}_k,\ k=1,\cdots,K$ as the k-th branch of the velocity and write

$$\Phi_{eu}^{\varepsilon}(t,\boldsymbol{x})=\int_{\mathbb{R}^n}\left(\frac{1}{2\pi\varepsilon}\right)^{\frac{n}{2}}r_{\theta}(\boldsymbol{x}-\boldsymbol{y})\sum_k\frac{\varphi_{eu}^{\varepsilon}(t,\boldsymbol{x},\boldsymbol{y},\boldsymbol{u}_k)}{|\det(\operatorname{Re}[\nabla_{\boldsymbol{\xi}}\phi]_{\boldsymbol{\xi}=\boldsymbol{u}_k})|}d\boldsymbol{y}. \tag{3.22}$$

Since $\det\left(\operatorname{Re}[\nabla_{\boldsymbol{\xi}}\phi]\right)=0$ at caustics, a direct numerical integration of (3.22) loses accuracy around singularities (see Example 3 in Sec. 5 for the detailed numerical demonstrations). To get a better accuracy, we split (3.22) into two parts

$$I_1=\sum_k\int_{L_1}\left(\frac{1}{2\pi\varepsilon}\right)^{\frac{n}{2}}r_{\theta}(\boldsymbol{x}-\boldsymbol{y})\frac{\varphi_{eu}^{\varepsilon}(t,\boldsymbol{x},\boldsymbol{y},\boldsymbol{u}_k)}{|\det(\operatorname{Re}[\nabla_{\boldsymbol{\xi}}\phi]_{\boldsymbol{\xi}=\boldsymbol{u}_k})|}d\boldsymbol{y}, \tag{3.23}$$

$$I_2=\sum_k\int_{L_2}\left(\frac{1}{2\pi\varepsilon}\right)^{\frac{n}{2}}r_{\theta}(\boldsymbol{x}-\boldsymbol{y})\frac{\varphi_{eu}^{\varepsilon}(t,\boldsymbol{x},\boldsymbol{y},\boldsymbol{u}_k)}{|\det(\operatorname{Re}[\nabla_{\boldsymbol{\xi}}\phi]_{\boldsymbol{\xi}=\boldsymbol{u}_k})|}d\boldsymbol{y}, \tag{3.24}$$

where

$$L_1=\left\{\boldsymbol{y}\Big|\big|\det(\operatorname{Re}[\nabla_{\boldsymbol{p}}\phi](t,\boldsymbol{y},\boldsymbol{p}_j))\big|\geq\tau\right\},$$

$$L_2=\left\{\boldsymbol{y}\Big|\big|\det(\operatorname{Re}[\nabla_{\boldsymbol{p}}\phi](t,\boldsymbol{y},\boldsymbol{p}_j))\big|<\tau\right\},$$

with τ being a small parameter. In the numerical simulation one needs to consider two facts about choosing the parameter τ:

1. to reduce the computational complexity one needs to make τ as small as possible to minimize the cost of computing (3.24);
2. for convenience, one needs to evaluate (3.23) easily by some quadrature rule using the mesh grid points.

See figure 4.7 (bottom) for example. The circles are the grid points we need to compute (3.23) and the cross points are the points we need to evaluate (3.24).

In our numerical simulations, I_1 is approximated by the trapezoid quadrature rule, while the singular integral I_2 is evaluated by the semi-Lagrangian method introduced in [19]. For convenience we summarize the semi-Lagrangian method here. Suppose we take a number of discrete beams centered at $\boldsymbol{y}^j$, $j = 1, \cdots, M_y$ with the velocity $\boldsymbol{u}_k^j$ on the contour. The idea is to trace each individual $(\boldsymbol{y}^j, \boldsymbol{u}_k^j)$ back to the initial position $(\boldsymbol{y}_0^j, \boldsymbol{u}_{k,0}^j)$ using (2.12)-(2.13) with $t \to -t$, then determine the weight function $\omega(\boldsymbol{y}_0^j)$ for it. For example, in one space dimension if the two adjacent points $y_0^{j_1}$ and $y_0^{j_2}$ of y_0^j satisfy $y_0^{j_1} < y_0^j < y_0^{j_2}$, then $\omega(y_0^j) = (y_0^{j_2} - y_0^{j_1})/2$ (see page 68 in [19] for details). In this process one gets rid of the singular term by noticing that $\mathrm{d}\boldsymbol{y}_0 = \dfrac{1}{|\det(\mathrm{Re}[\nabla_{\boldsymbol{\xi}}\phi]_{\boldsymbol{\xi}=\boldsymbol{u}_k})|}\mathrm{d}\boldsymbol{y}$. The discrete form of (3.24) reads as

$$\widetilde{I}_2 = \sum_{j=1}^{M_y}\sum_k \left(\frac{1}{2\pi\varepsilon}\right)^{\frac{n}{2}} r_\theta(\boldsymbol{x}-\boldsymbol{y}^j)\varphi_{eu}^\varepsilon(t,\boldsymbol{x},\boldsymbol{y}^j,\boldsymbol{u}_k^j)\omega(\boldsymbol{y}_0^j). \qquad (3.25)$$

We remark here that the semi-Lagrangian method (3.25) can be used to evaluate (3.22), as was done in [19]. However, when the rays diverge backward in time, $\omega(\boldsymbol{y}_0^j)$ becomes large. The local semi-Lagrangian method helps to reduce such errors.

REMARK 3.4. When the velocity contours are complicated due to large numbers of caustics, the implementation of this local semi-Lagrangian method is difficult. In these cases we refer to a discritized delta function method [33] for numerically computing (3.21) which does not contain the singular denominator. In this method, one needs to compute (3.6) for solving the phase function since all the function values near the support domain of the delta functions $\delta(\mathrm{Re}[\phi_j])$ are needed to evaluate (3.21). This will be studied in a forthcoming work.

3.4. Estimates on computational complexity. Since the errors of the Gaussian beam method were already discussed in [24, 30], we only focus on the analysis of the computational complexity here. There are two steps for computing the Gaussian beam solution.

1. Solving the PDEs (3.5) and (3.9).
2. Constructing the asymptotic solution using (3.22).

The numerical cost of the first step is related to the mesh size and the time step. We will show later that the optimal mesh size is $\Delta\boldsymbol{y} = O(\varepsilon^{\frac{1}{2}})$ in the numerical simulations. We denote the numerical error of solving the PDEs as E_{num}, which introduces the error of E_{num}/ε when one constructs φ_{eu}^ε in (3.20). For this error to be minor, we require the time step taken as $\Delta t \sim \varepsilon^{\frac{1}{2}}$ in a fourth order time discretization. Then the computational complexity of the first step is $O(\varepsilon^{-\frac{n+1}{2}}\ln\varepsilon^{-\frac{1}{2}})$ if the local level set method is used.

The numerical cost of the second step is related to the number of nodes $N_{\boldsymbol{x}}$ in the $\boldsymbol{x}$-mesh when we finally construct the solution by (3.22). To get the *whole wave field*, one needs to resolve the wave length, which requires $N_{\boldsymbol{x}} \sim \varepsilon^{-n}$. Due to the truncation

function $r_\theta(\boldsymbol{x}-\boldsymbol{y})$ and the fact that the imaginary part of the Hessian matrix M is positive definite by Theorem 3.2, the computational cost of (3.23) is $O(1)$ for each $\boldsymbol{x}$. The computational cost of each backtrace is $O(\varepsilon^{-\frac{1}{2}})$ in the semi-Lagrangian method for solving (3.24). However, since (3.24) is an integration on a small local domain (τ is small), the computational cost of (3.25) is negligible compared to the rest. If the discretized delta function method [33] is used to evaluate (3.21), the computational cost for each x is still $O(1)$ because of the truncation function $r_\theta(\boldsymbol{x}-\boldsymbol{y})$ and the fact that each beam decays exponentially. So the total computational complexity of the second step is $O(\varepsilon^{-n})$ for computing the *whole wave field*.

In summary, the total computational cost is $O(\varepsilon^{-\frac{n+1}{2}}\ln\varepsilon^{-\frac{1}{2}}+\varepsilon^{-n})$. We remark that the computational cost mainly comes from solving the Liouville equations, which is $O(\varepsilon^{-\frac{n+1}{2}}\ln\varepsilon^{-\frac{1}{2}})$, if only some *selected points* in the wave field are needed to be computed. This is better than the complexity of directly solving the Schrödinger Equation (1.1)-(1.2) using the Time Splitting Spectral Method [1], which is $O(\varepsilon^{-n-1/2}\ln\varepsilon^{-n})$.

4. The numerical examples

In this section, we present several numerical examples using both the Lagrangian and the Eulerian formulations to show the accuracy of the Gaussian beam solutions and the numerical efficiency. We compute the solution of the Schrödinger equation by the Strang splitting spectral method [1]. The 'exact' Schrödinger solution Ψ^ε is obtained by using a very fine mesh and a very small time step with an appropriately large domain so that the periodic boundary condition does not introduce a significant error to the initial value problem. Since all of the Gaussian beams are observed to be narrow in the numerical examples, the truncation parameter θ in (2.29) and (3.22) is chosen large enough so that the cut-off error is almost zero. We gain convergence rates higher than $O(\sqrt{\varepsilon})$ in the numerical simulation because of the error cancellations in the summation of Gaussian beams (see [24]).

4.1. The Lagrangian Gaussian beam examples.   We study the Lagrangian formulation numerically in this subsection. The numerical examples are chosen such that the fourth order Runger-Kutta scheme with the time step $\Delta t \sim \varepsilon^{1/2}$ is good to be used for solving (2.12)–(2.16). We analyze the asymptotic expansion error and the initial condition error in Example 1. The numerical integration errors and the errors of the ODE solvers are discussed in Example 2.

Example 1: A free particle with zero potential $V(x)=0$. The initial conditions for the Schrödinger equation are given by

$$A_0(x)=e^{-25(x-0.5)^2}, \, S_0(x)=-x^2.$$

In this example, the Gaussian beam solution (2.28) can be solved analytically

$$\Phi_{la}^\varepsilon(t,x)=\frac{e^{-6.25-\frac{x^2}{2\varepsilon(5t^2-4t+1)}+\frac{i}{\varepsilon}\frac{(5t-2)x^2}{2(5t^2-4t+1)}+\frac{B^2}{4A}}}{\sqrt{2A\varepsilon\big((-2+i)t+1\big)}},$$

where A and B are

$$A=25+\frac{(1-2t)^2}{2\varepsilon(5t^2-4t+1)}-\frac{(1-2t)t}{2\varepsilon(5t^2-4t+1)}i,$$

$$B=25+\frac{2(1-2t)x}{2\varepsilon(5t^2-4t+1)}-\frac{xt}{\varepsilon(5t^2-4t+1)}i.$$

In this example the initial velocity contour is a straight line with the slope of -1. As time increases the slope steepens and becomes infinity at $t=0.5$ which generates an instantaneous caustic. After $t=0.5$ the slope becomes positive and the caustic disappears. This type of caustic is different from the cusp caustic which will be studied in Examples 2 and 3. As a consequence, we observed a higher convergence rate in l^1 norm than in the other examples.

We plot the solutions at time $t=0.5$ when the caustic is generated in figure 4.1. We compare the wave amplitudes between the Gaussian beam solution $\Phi_{la}^{\varepsilon}(t,x)$ and the Schrödinger solution $\Psi^{\varepsilon}(t,x)$ for different ε. The error comes mostly from the asymptotic expansion and the initial data approximation.

The l^1, l^2 and l^∞ errors between Φ_{la}^{ε} and Ψ^{ε} for different ε are plotted in figure 4.2. One can see that the Gaussian beam solution Φ_{la}^{ε} converges in ε with an order of about 1.5 in the l^1 norm, one in the l^2 norm, and one half in the l^∞ norm.

Example 2: Consider the potential $V(x)=2x^3$, with the initial conditions

$$A_0(x)=e^{-25x^2}, \; S_0(x)=\frac{1}{\pi}\cos(\pi x).$$

This example deals with a variable potential case. Since the potential $V(x)=2x^3$ makes the force *one-directional*, the wave function of (1.1)-(1.2) is *asymmetric*. Two caustics form at time $t=0.5$.

We use the fourth order Runge-Kutta method to solve the ODE system (2.12)–(2.16) with the initial data (2.23)–(2.27) in the interval $[-1.5,1.5]$ with periodic boundary conditions. Note that the Hessian M and the amplitude A are solved via the dynamic ray tracing system (2.17), (2.19) and (2.20). In Table 4.1, we present the l^1, l^2 and l^∞ errors between Φ^{ε} and Ψ^{ε} using different Δt and $N_{y_0}=200$. We draw the conclusion that the numerical errors are negligible compared to the other types of errors when $\Delta t \leq 0.02$ for $\varepsilon = \frac{1}{4096}$, $n=1$.

Next we study the error coming from evaluating the integral (2.28) numerically. Evidently, the more nodes of y_0 are used, the more accurate the numerical integration will be; however, each node of y_0 corresponds to an ODE system, thus a large number of nodes will result in a high computational cost. In this example, we investigate the accuracy versus N_{y_0} for $\varepsilon \ll 1$. We also study the optimal relation between N_{y_0} and ε which ensures a good approximation and low computational cost.

We plot the solutions at time $t=0.5$ in figure 4.3. The wave amplitudes are compared between the Schrödinger solution Ψ^{ε} and the Gaussian beam solution Φ^{ε} using different numbers of beams N_{y_0} at $\varepsilon = \frac{1}{4096}$. The l^1, l^2 and l^∞ errors between Φ^{ε} and Ψ^{ε} are given in Table 4.2. We can see that the Gaussian beam solution converges quickly with the increasing number of beams. In figure 4.4 (left), we show that $N_{y_0} \sim \varepsilon^{-\frac{1}{2}}$ is pretty much enough, and larger N_{y_0} will not reduce the error further since the other errors start to dominate.

figure 4.4 (right) gives the l^1, l^2 and l^∞ errors between Φ_{la}^{ε} and Ψ^{ε} for different ε at time $t=0.5$, where we use $N_{y_0}=800$ and $\Delta t=0.001$. The convergence rate of the error in ε is about first order in l^1 and l^2 norms, the order of 0.7894 in the l^∞ norm. We also plot the comparisons of the position density, the density flux and the kinetic energy for $\varepsilon = \frac{1}{4096}$, using $N_{y_0}=200$, $t=0.5$ and $\Delta t=0.01$ in figure 4.5.

4.2. The Eulerian Gaussian beam examples.   In this subsection, we study the Gaussian beam method numerically using the Eulerian formulation. The numerical methods to the Liouville equation are very mature. It could be solved by
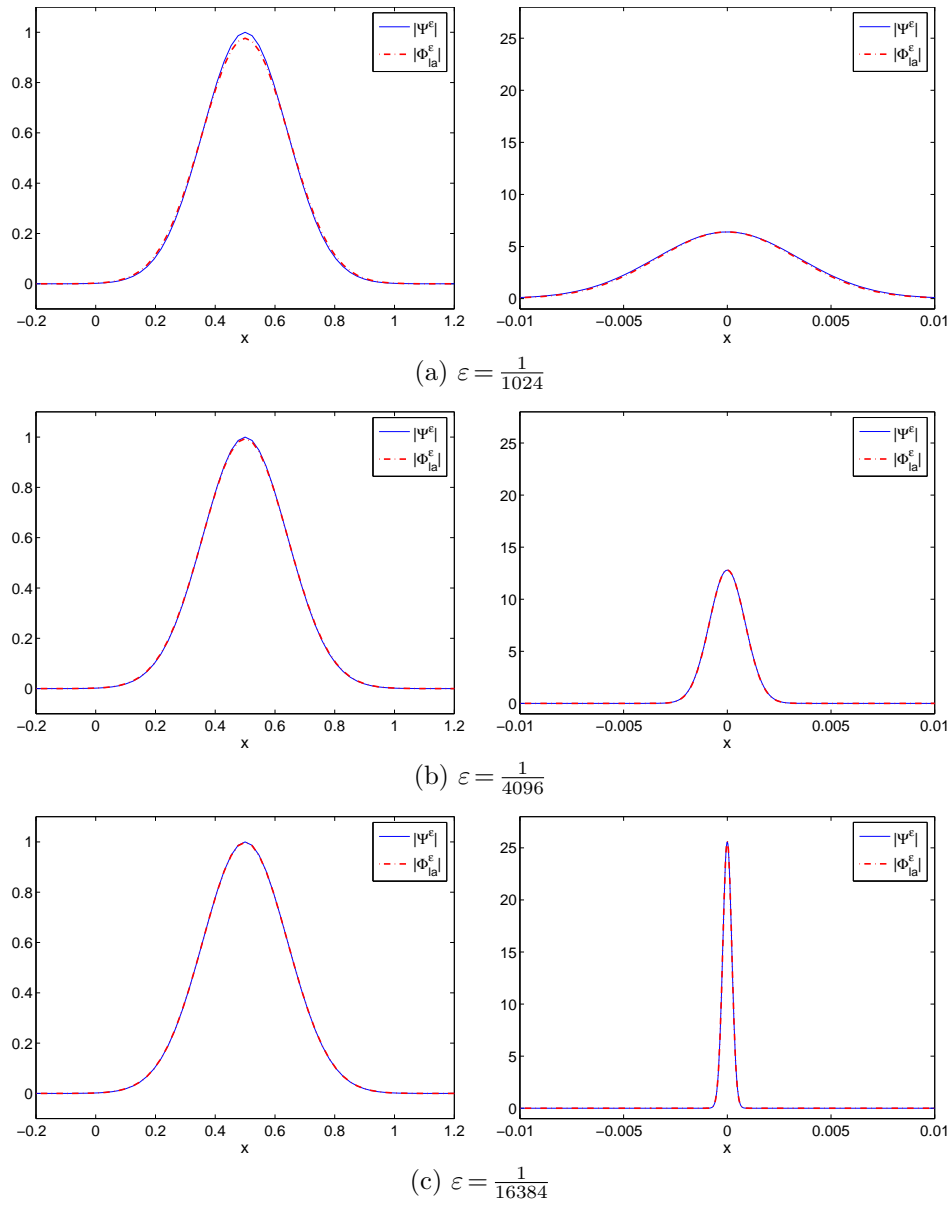
(a) $\varepsilon = \frac{1}{1024}$

(b) $\varepsilon = \frac{1}{4096}$

(c) $\varepsilon = \frac{1}{16384}$

FIG. 4.1. *Example 1: the Schrödinger solution $|\Psi^\varepsilon|$ versus the Gaussian beam solution $|\Phi_{la}^\varepsilon|$ at different ε. The left figures are the comparisons at $t=0$ (the initial time); the right figures are the comparisons at time $t=0.5$.*

Δt	0.04	0.02	0.01	0.005
$\|\Phi_{la}^\varepsilon - \Psi^\varepsilon\|_1$	7.88×10^{-2}	4.18×10^{-4}	4.18×10^{-4}	4.18×10^{-4}
$\|\Phi_{la}^\varepsilon - \Psi^\varepsilon\|_2$	3.51×10^{-1}	1.68×10^{-3}	1.68×10^{-3}	1.68×10^{-3}
$\|\Phi_{la}^\varepsilon - \Psi^\varepsilon\|_\infty$	2.58×10^{0}	1.24×10^{-2}	1.24×10^{-2}	1.24×10^{-2}

TABLE 4.1. *the l^1, l^2 and l^∞ errors for different Δt for Example 2.*
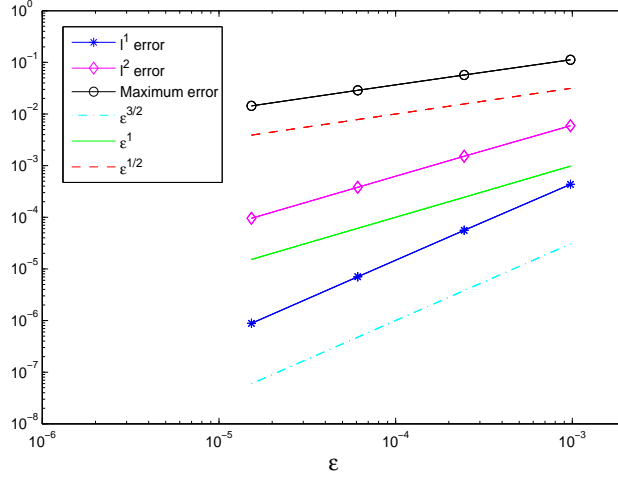
FIG. 4.2. *Example 1: the convergence rate in ε of the l^1, l^2 and l^∞ errors of the wave function.*

N_{y_0}	50	100	150	200
$\|\Phi_{la}^\varepsilon - \Psi^\varepsilon\|_1$	2.72×10^{-2}	6.92×10^{-4}	4.18×10^{-4}	4.18×10^{-4}
$\|\Phi_{la}^\varepsilon - \Psi^\varepsilon\|_2$	1.09×10^{-1}	2.69×10^{-3}	1.68×10^{-3}	1.68×10^{-3}
$\|\Phi_{la}^\varepsilon - \Psi^\varepsilon\|_\infty$	7.10×10^{-1}	2.02×10^{-2}	1.24×10^{-2}	1.24×10^{-2}

TABLE 4.2. *the l^1, l^2 and l^∞ errors at $\varepsilon = \frac{1}{4096}$ for different N_{y_0} for Example 2.*

either the finite difference method [16, 17] or the semi-Lagrangian method [19, 20]. We do not address the issue of an optimal Liouville solver here.

We present two numerical examples to show the effectiveness of the Eulerian Gaussian beams method. In Example 3 (first proposed in [16]), we point out that around the caustics one needs to take enough discrete beams to resolve the velocity contour well to obtain a good accuracy. This is an issue not discussed in [19]. We also study a simple two-dimensional case in Example 4 which first appeared in [26].

Example 3 (1D) **:** Free motion particles with zero potential $V(x) = 0$. The initial conditions for the Schrödinger equation are given by

$$A_0(x) = e^{-25x^2}, \ S_0(x) = -\frac{1}{5}\log(2\cosh(5x)),$$

which implies that the initial density and velocity are

$$\rho_0(x) = |A_0(x)|^2 = \exp(-50x^2), \qquad u_0(x) = \partial_x S_0(x) = -\tanh(5x).$$

The solutions of the Liouville equations (3.5), (3.6) and (3.9) can be solved by the method of characteristics analytically:

$$\phi(t,y,\xi) = \phi_0(y - \xi t, \xi),$$
$$S(t,y,\xi) = S_0(y - \xi t) + t u_0^2(y - \xi t)/2,$$
$$f(t,y,\xi) = A_0^2(y - \xi t, \xi).$$
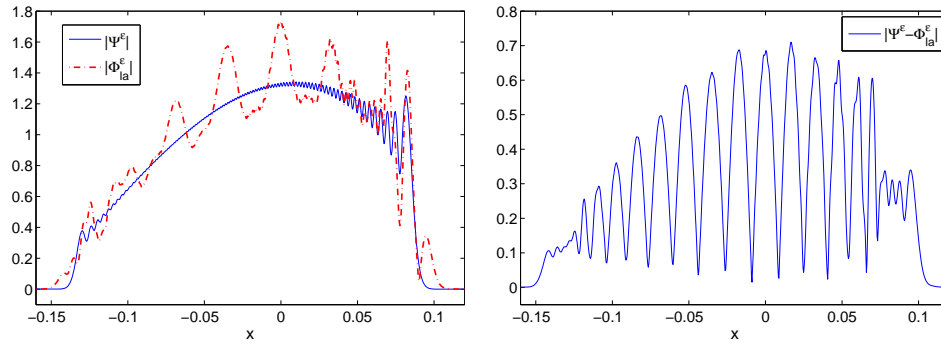
(a) $N_{y_0} = 50$
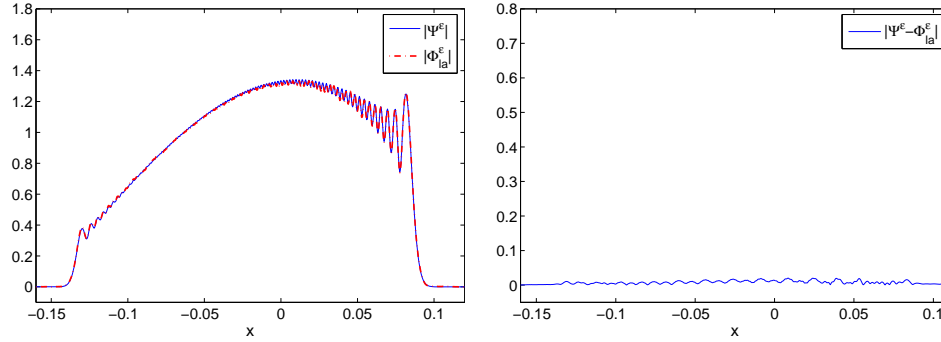
(b) $N_{y_0} = 100$
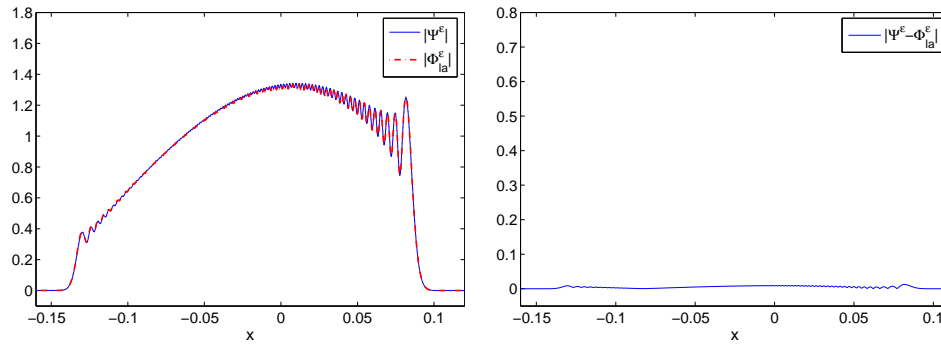
(c) $N_{y_0} = 200$

FIG. 4.3. *Example 2: the Schrödinger solution $|\Psi^\varepsilon|$ versus the Gaussian beams solution $|\Phi^\varepsilon_{la}|$ at $\varepsilon = \frac{1}{4096}$ using different N_{y_0}. The left figures are the comparisons at $t = 0.5$; the right figures plot the errors $|\Psi^\varepsilon - \Phi^\varepsilon_{la}|$.*

We use $\Delta y = \Delta \xi = 0.002$ in the mesh for the Eulerian beam simulation, and take $\Delta x = \dfrac{1}{65536}$, the same mesh size as the numerical solution to the Schrödinger equation, to construct the wave function (3.22). figure 4.6 shows the comparison of the wave amplitude between the Schrödinger solution Ψ^ε and the Eulerian beams solution Φ^ε_{eu} for $\varepsilon = 1 \times 10^{-4}$ and at $t = 0.5$.

From the left figures of figure 4.6(a)-(c), one can see that summing up the beams
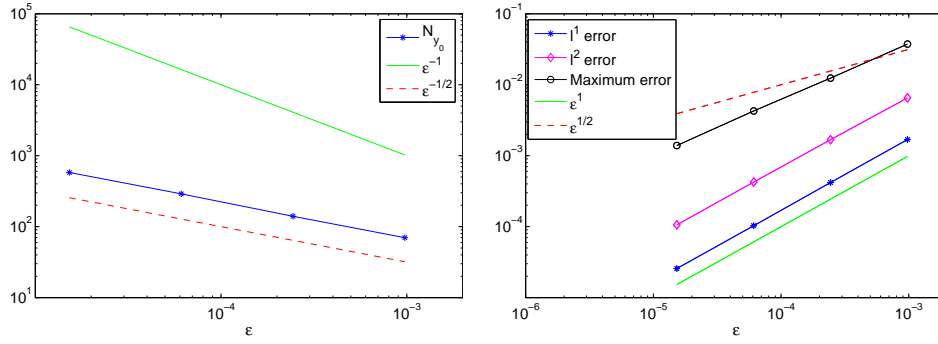
FIG. 4.4. *Example 2. Left: the plot of the optimal beam number N_{y_0} for each ε. Right: the convergence rate in ε of the l^1, l^2 and l^∞ errors of the wave function.*

centered on the mesh could only approximate the Schrödinger solution accurately *away* from the caustics. In order to make good approximations *around* the caustics, one has to sum up more beams whose centers better represent the velocity contour curve. In other words, one needs to numerically resolve the singular integration (3.24) accurately by the semi-Lagrangian method. This process could be easily implemented by the Matlab subroutine 'contour'. The results are shown in the right figures of figure 4.6(a)–(c). To make some comparisons we list other types of asymptotic solutions in figure 4.6(d)–(f) given by geometric optics [16] and the corrected geometric optics with phase shift information (Keller-Maslov index) [17]. Since both the approximations blow up at caustics, we make some truncations when plot them. One could also notice that the Eulerian beam solution Φ_{eu}^ε naturally carries the phase shift information even when the velocity contour is not well resolved. The error of Φ_{eu}^ε is substantially smaller than Φ_{GO}^ε and Φ_{PS}^ε around the caustics.

We give the velocity contour and beam distribution around one caustic in figure 4.7. This figure shows that the contour of velocity around the caustic (near $x = -0.18$) was not resolved well, which causes large errors around the caustic shown in figure 4.6(c) (left). Figure 4.8 (left) shows the convergence rates in ε of amplitude are of order 0.9082 in the l^1 norm, order 0.8799 in l^2 norm and order 0.7654 in the l^∞ norm. In figure 4.8 (right), we numerically show that the optimal relationship between Δy and ε is $\Delta y \sim \varepsilon^{1/2}$, which ensures a good approximation.

Example 4 (2D): Take the potential $V(x_1, x_2) = 10$ and the initial conditions of the Schrödinger equation as

$$A_0(x_1, x_2) = e^{-25(x_1^2 + x_2^2)},$$
$$S_0(x_1, x_2) = -\frac{1}{5}(\log(2\cosh(5x_1)) + \log(2\cosh(5x_2))).$$

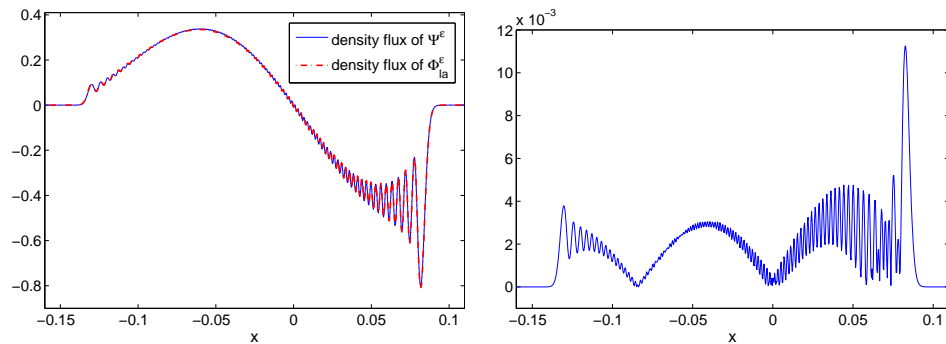Then the initial density and two components of the velocity are

$$\rho_0(x_1, x_2) = \exp(-50(x_1^2 + x_2^2)),$$

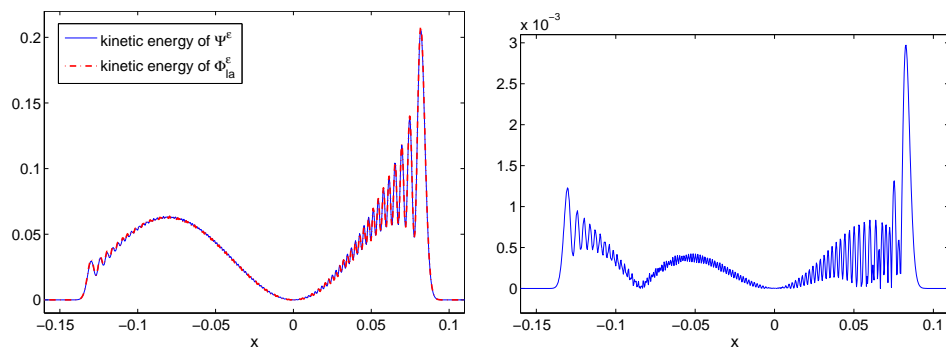$$u_0(x_1, x_2) = -\tanh(5x_1), \quad v_0(x_1, x_2) = -\tanh(5x_2).$$

This is an easily implemented two-dimensional example, since the two components are either x_1-isotropic or x_2-isotropic (see figure 4.9). More complicated examples
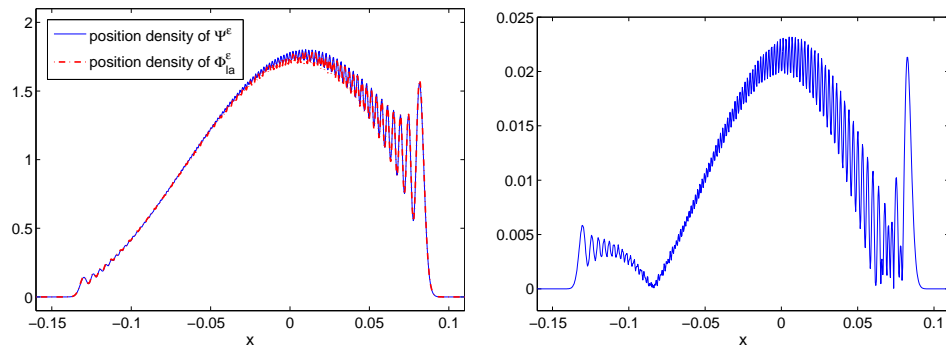
(a) The position density


(b) The density flux

(c) The kinetic energy

FIG. 4.5. *Example 2:* $\varepsilon = \frac{1}{4096}$, $N_{y_0} = 200$, $t = 0.5$ *and* $\Delta t = 0.01$. *The left figures are the comparisons of the position density, the density flux and the kinetic energy of the Schrödinger solution Ψ^ε and the Gaussian beams solution Φ^ε_{la} at $t = 0.5$; the right figures show the errors between them.*

could be dealt with similarly, but one needs more sophisticated interpolation techniques to get the intersection of the zero-level contours. We do not address this issue here and refer to [23] for interested readers. We use $\Delta y_1 = \Delta y_2 = \Delta \xi_1 = \Delta \xi_2 = 0.004$ for the computation of the Liouville equations (3.5) and (3.9) by the semi-Lagrangian method [19, 20]. The mesh size is $\Delta x_1 = \Delta x_2 = \dfrac{1}{65536}$ for the construction of the
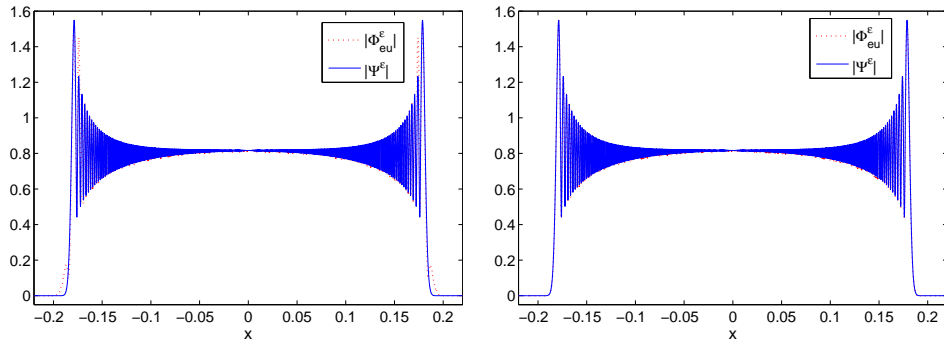
(a) Comparison of wave amplitude
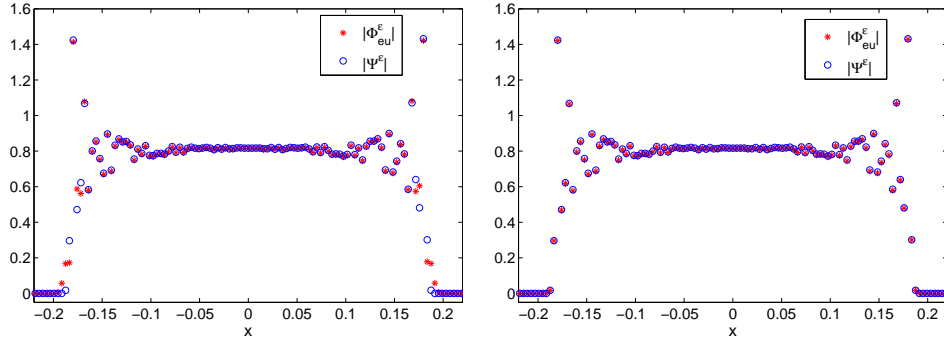
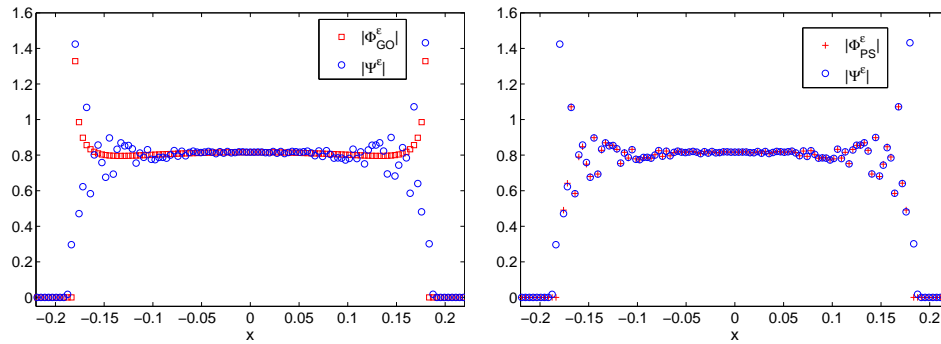(b) Comparison of undersampled wave amplitude
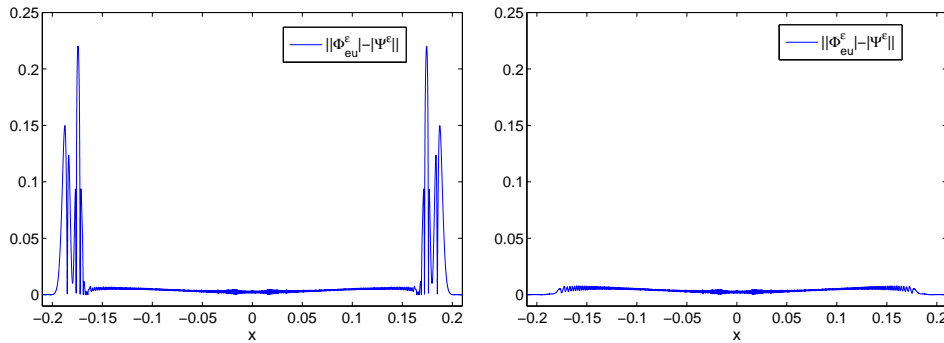
(c) Errors

FIG. 4.6. *Example 3:* $\varepsilon = 1 \times 10^{-4}$. *The figure shows the comparison of the wave amplitudes between the Eulerian beam solution* Φ_{eu}^ε *and the Schrödinger solution* Ψ^ε *at* $t = 0.5$. *The Eulerian beam solution on the left is obtained by the summation of all the beams centered on the mesh, and the one on the right is obtained by the summation of the beams which better resolve the zero contour curve around caustics.*

Eulerian beam solution (3.22). We take $\varepsilon = 0.001$ and compare the wave amplitudes of the Schrödinger solution Ψ^ε and the Eulerian beam solution Φ_{eu}^ε in figure 4.10 at time $t = 0.5$. The error between them is shown in figure 4.11.
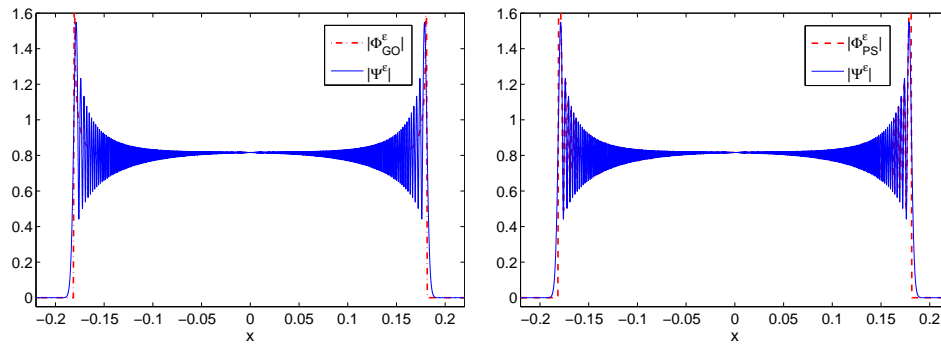
(d) Comparison of wave amplitude

(e) Comparison of undersampled wave amplitude
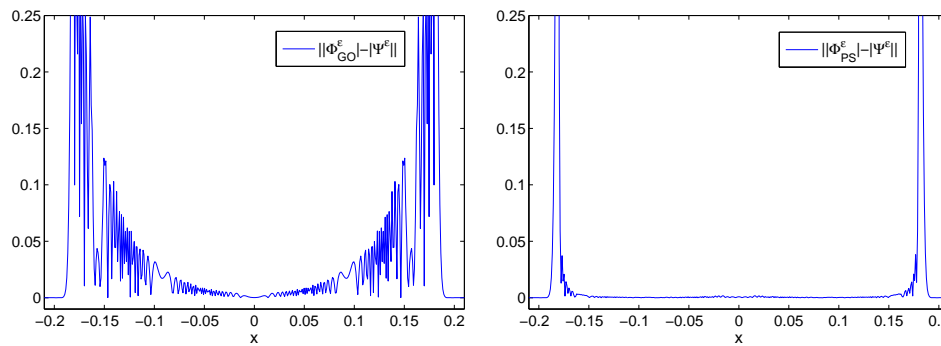
(f) Errors

FIG. 4.6. *(continued). Left: the comparison between the geometric optics approximation* Φ_{GO}^{ε} *and the Schrödinger solution* Ψ^{ε}; *right: the comparison between the geometric optics corrected with phase shift (Keller-Maslov index)* Φ_{PS}^{ε} *and the Schrödinger solution* Ψ^{ε}.

5. Conclusion

In this paper, we present the Lagrangian and Eulerian formulations of the Gaussian beam method for solving the Schrödinger equation. A new Eulerian Gaussian beam method is developed using the level set method. By using observation (3.3), we evaluate the Hessian matrix of the phase directly from the first derivatives of the (complexified) level set function for velocity, and thus avoid using an extra $2n^2$ (for
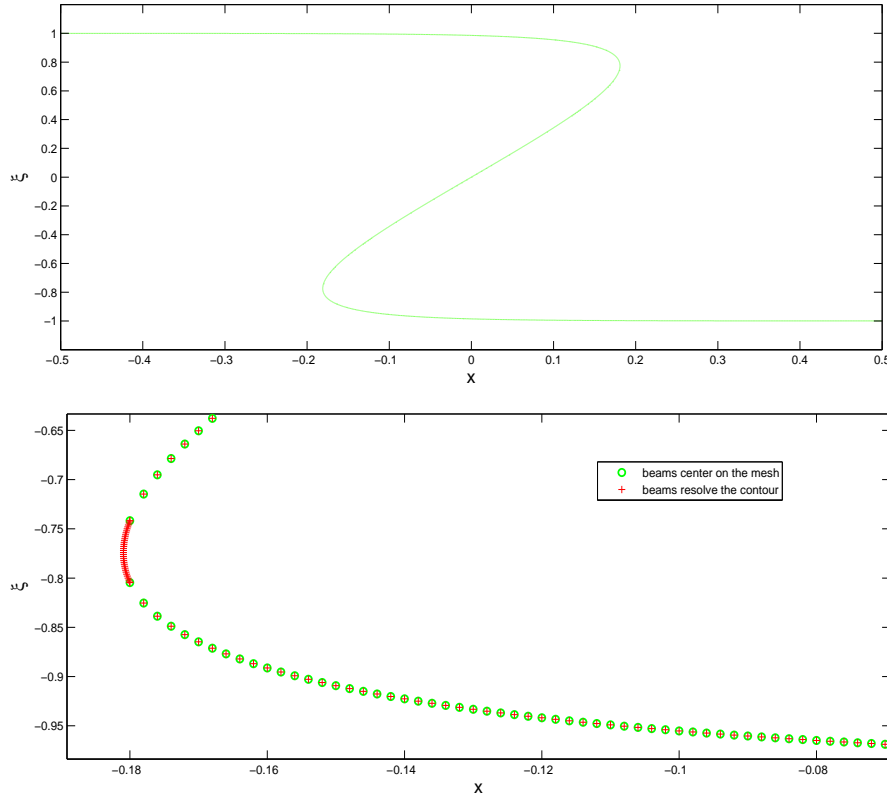
FIG. 4.7. *Example 3: t=0.5. The top figure shows the multivalued velocity; the bottom figure shows the beams centered on the mesh and the beams needed to resolve the zero contour around the caustic point. The former case does not resolve the caustic around $x=-0.18$ well, and thus causes errors shown in figure 4.6(c) (left).*
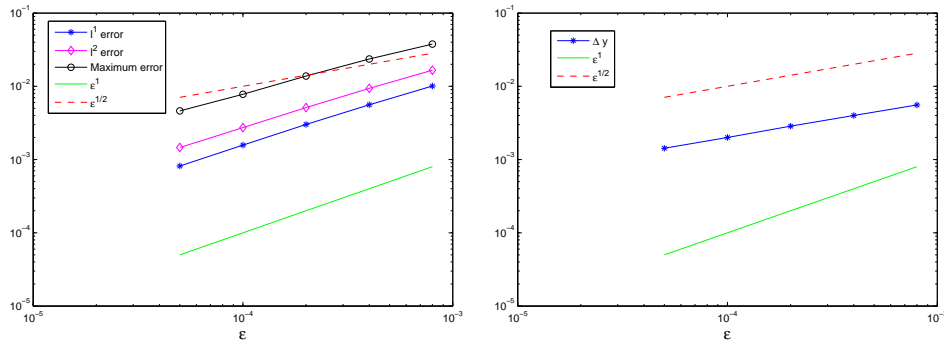

FIG. 4.8. *Example 3. Left: the convergence rates in ε of the l^1, l^2 and l^∞ errors of the wave amplitude; right: the plot of the optimal Δy for each ε.*

n space dimensions) complex-valued inhomogeneous Liouville equations as was done in [19]. We verify the accuracy of the Gaussian beam solutions by several numerical examples which show small error around caustics. We also point out that one needs
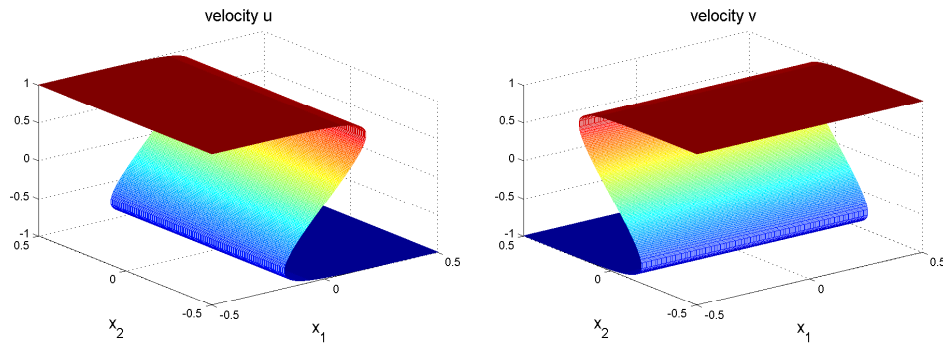
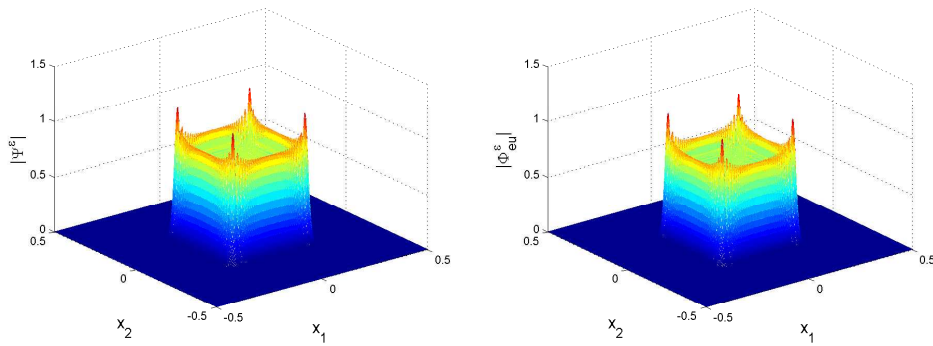FIG. 4.9. *Example 4: the two components of the multivalued velocity at $t = 0.5$.*

FIG. 4.10. *Example 4: the comparison of the wave amplitude between the Schrödinger solution Ψ^ε on the left and the Eulerian beams solution Φ^ε_{eu} on the right for $\varepsilon = 0.001$ and at $t = 0.5$.*

to resolve the velocity contour near caustics to obtain good approximations in the Eulerian formulation. Moreover, we give a numerical criteria for the optimal choice of the beam numbers in the Gaussian beam summation. We will extend this method to other problems in high frequency waves in the near future.
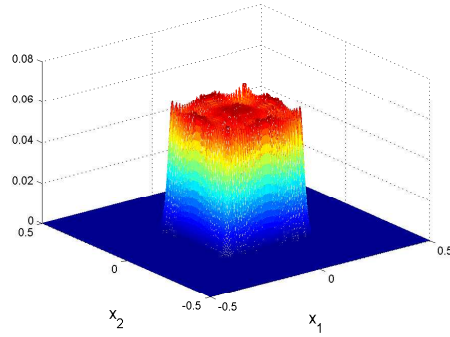
Acknowledgement. Xu Yang would like to thank Prof. Björn Engquist and Prof. Richard Tsai for the kind invitation to the workshop on Gaussian beams held in ICES, Austin, TX, which stimulated his interest in this subject.

Appendix A. The Lagrangian summation formulation (2.28) reads as

$$\Phi^\varepsilon_{la}(t, \boldsymbol{x}) = \int_{\mathbb{R}^n} \left(\frac{1}{2\pi\varepsilon} \right)^{\frac{n}{2}} r_\theta(\boldsymbol{x} - \boldsymbol{y}(t, \boldsymbol{y}_0)) \varphi^\varepsilon_{la}(t, \boldsymbol{x}, \boldsymbol{y}_0) \mathrm{d}\boldsymbol{y}_0, \tag{A.1}$$

which is equivalent to

$$\Phi^\varepsilon_{eu}(t, \boldsymbol{x}) = \int_{\mathbb{R}^n} \int_{\mathbb{R}^n} \left(\frac{1}{2\pi\varepsilon} \right)^{\frac{n}{2}} r_\theta(\boldsymbol{x} - \boldsymbol{y}) \varphi^\varepsilon_{eu}(t, \boldsymbol{x}, \boldsymbol{y}, \boldsymbol{p}) \delta(\mathrm{Re}[\boldsymbol{\phi}](0, \boldsymbol{y}_0, \boldsymbol{p}_0)) \mathrm{d}\boldsymbol{p}_0 \mathrm{d}\boldsymbol{y}_0, \tag{A.2}$$

FIG. 4.11. *Example 4: the error plot of* $||\Psi^\varepsilon| - |\Phi_{eu}^\varepsilon||$.

based on $\text{Re}[\nabla_{\boldsymbol{p}_0}\boldsymbol{\phi}](0,\boldsymbol{y}_0,\boldsymbol{p}_0) = I$. Note that the integrated variables $\boldsymbol{y}_0,\boldsymbol{p}_0$ are the initial positions of $\boldsymbol{y},\boldsymbol{p}$. Changing variables by $\boldsymbol{y},\boldsymbol{p}$, we get

$$\Phi_{eu}^\varepsilon(t,\boldsymbol{x}) = \int_{\mathbb{R}^n}\int_{\mathbb{R}^n}\left(\frac{1}{2\pi\varepsilon}\right)^{\frac{n}{2}} r_\theta(\boldsymbol{x}-\boldsymbol{y})\varphi_{eu}^\varepsilon(t,\boldsymbol{x},\boldsymbol{y},\boldsymbol{p})\delta(\text{Re}[\phi](t,\boldsymbol{y},\boldsymbol{p}))\mathrm{d}\boldsymbol{p}\mathrm{d}\boldsymbol{y}, \qquad \text{(A.3)}$$

in which we need $\det J = 1$ for

$$J = \begin{pmatrix} \nabla_{\boldsymbol{y}_0}\boldsymbol{y} & \nabla_{\boldsymbol{p}_0}\boldsymbol{y} \\ \nabla_{\boldsymbol{y}_0}\boldsymbol{p} & \nabla_{\boldsymbol{p}_0}\boldsymbol{p} \end{pmatrix}.$$

First it is easy to see $\det J|_{t=0} = 1$. Moreover,

$$\frac{\mathrm{d}J}{\mathrm{d}t} = UJ,$$

with $U = \begin{pmatrix} 0 & I \\ -\nabla_{\boldsymbol{y}}^2 V & 0 \end{pmatrix}$. This gives

$$\frac{\mathrm{d}}{\mathrm{d}t}(\det J) = \text{tr}(\text{adj}(J)\frac{\mathrm{d}J}{\mathrm{d}t}) = \text{tr}(\text{adj}(J)UJ) = \text{tr}(UJ\text{adj}(J)) = \det(J)\text{tr}(U) = 0,$$

where $\text{adj}(J) = (\det J)J^{-1}$.

REFERENCES

[1] W. Bao, S. Jin and P.A. Markowich, *On time-splitting spectral approximations for the Schrödinger equation in the semiclassical regime*, J. Comput. Phys., 175(2), 487–524, 2002.

[2] J.D. Benamou, *Big ray tracing: Multivalued travel time field computation using viscosity solutions of the eikonal equation*, J. Comp. Phys., 128, 463–474, 1996.

[3] J.D. Benamou, *Direct computation of multivalued phase space solutions for Hamilton-Jacobi equations*, Comm. Pure Appl. Math., 52, 1443–1457, 1999.

[4] V. Cerveny, M.M. Popov and I. Psencik, *Computation of wave fields in inhomogeneous media - Gaussian beam approach*, Geophys. J. R. Astr. Soc., 70, 109–128, 1982.

[5] L.-T. Cheng, H. Liu, and S. Osher, *Computational high-frequency wave propagation using the level set method, with applications to the semi-classical limit of Schrödinger equations*, Commun. Math. Sci., 1(3), 593–621, 2003.

[6] R. Courant and D. Hilbert, *Methods of Mathematical Physics*, Vol. II, Interscience Publishers, 1962.

[7] L. Dieci and T. Eirola, *Preserving monotonicity in the numerical solution of Riccati differential equations*, Numer. Math., 74(1), 35–47, 1996.

[8] B. Engquist and O. Runborg, *Computational high frequency wave propagation*, Acta Numerica, 12, 181–266, 2003.

[9] B. Engquist, O. Runborg and A.K. Tornberg, *High frequency wave propagation by the segment projection method*, J. Comp. Phys., 178, 373–390, 2002.

[10] L. Gosse, *Using K-branch entropy solutions for multivalued geometric optics computations*, J. Comput. Phys., 180(1), 155–182, 2002.

[11] L. Gosse, S. Jin and X.T. Li, *On two moment systems for computing multiphase semiclassical limits of the Schrödinger equation*, Math. Models Meth. Appl. Sci., 13(12), 1689–1723, 2003.

[12] N.R. Hill, *Gaussian beam migration*, Geophysics, 55(11), 1416–1428, 1990.

[13] N.R. Hill, *Prestack Gaussian-beam depth migration*, Geophysics, 66(4), 1240–1250, 2001.

[14] S. Jin and X.T. Li, *Multi-phase computations of the semiclassical limit of the Schrödinger equation and related problems: Whitham vs. Wigner*, Physica D, 182, 46–85, 2003.

[15] S. Jin, H. Liu, S. Osher and R. Tsai, *Computing multi-valued physical observables the semiclassical limit of the Schrödinger equations*, J. Comp. Phys., 205, 222–241, 2005.

[16] S. Jin and S. Osher, *A level set method for the computation of multivalued solutions to quasilinear hyperbolic PDEs and Hamilton-Jacobi equations*, Commun. Math. Sci., 1(3), 575–591, 2003.

[17] S. Jin and X. Yang, *Computation of the semiclassical limit of the Schrödinger equation with phase shift by a level set method*, J. Sci. Comp., 35(2–3), 144–169, 2008.

[18] S. Leung and J. Qian, *Eulerian Gaussian beams for Schrödinger equations in the semi-classical regime*, preprint.

[19] S. Leung, J. Qian and R. Burridge, *Eulerian Gaussian beams for high-frequency wave propagation*, Geophysics, 72(5), 61–76, 2007.

[20] S. Leung, J. Qian and S. Osher, *A level set method for three dimensional paraxial geometrical optics with multiple sources*, Commun. Math. Sci., 2(4), 643–672, 2004.

[21] P.A. Markowich, P. Pietra and C. Pohl, *Numerical approximation of quadratic obaservables of Schrödinger-type equations in the semiclassical limit*, Numer. Math., 81, 595–630, 1999.

[22] P.A. Markowich, P. Pietra, C. Pohl and H.P. Stimming, *A wigner-measure analysis of the Dufort-Frankel scheme for the Schrödinger equation*, SIAM J. Num. Anal., 40, 1281–1310, 2002.

[23] C. Min, *Simplicial isosurfacing in arbitrary dimension and codimension*, J. Comp. Phys., 190(1), 295–310, 2003.

[24] M. Motamed and O. Runborg, *Taylor expansion errors in Gaussian beam summation*, preprint.

[25] M. Motamed and O. Runborg, *A wave front-based Gaussian beam method for computing high frequency waves*, preprint.

[26] S. Osher, L.-T. Cheng, M. Kang, H. Shim and Y.-H. Tsai, *Geometric optics in a phase-space-based level set and Eulerian framework*, J. Comput. Phys., 179(2), 622–648, 2002.

[27] D. Peng, B. Merriman, S. Osher, H. Zhao and M. Kang, *A PDE based fast local level set method*, J. Comput. Phys., 155, 410–438, 1999.

[28] M.M. Popov, *A new method of computation of wave fields using Gaussian beams*, Wave Motion, 4, 85–97, 1982.

[29] J. Ralston, *Gaussian beams and the propagation of singularities*, Studies in PDEs, MAA stud. Math., 23, 206–248, 1982.

[30] N.M. Tanushev, *Superpositions and higher order Gaussian beams*, Commun. Math. Sci., 6(2), 449–475, 2008.

[31] N.M. Tanushev, J.L. Qian and J. Ralston, *Mountain waves and Gaussian beams*, SIAM Multiscale Modeling and Simulation, 6, 688–709, 2007.

[32] V. Vinje, E. Iversen and H. Gjøystdal, *Traveltime and amplitude estimation using wavefront construction*, Geophysics, 58(8), 1157–1166, 1993.

[33] X. Wen, *High order numerical methods to two dimensional delta function integrals in level set methods*, preprint.

[34] G.B. Whitham, *Linear and Nonlinear Waves*, Wiley, New York, 1974.